Nature Communications

https://doi.org/10.1038/s41467-026-73677-x

Article in Press

Deciphering cytokine-driven ADP-ribosylation signaling networks via Af1521-based mass spectrometry analysis of labile Glu/Asp-linkages

Received: 10 November 2025

Accepted: 19 May 2026

Cite this article as: Buch-Larsen, S.C., Hendriks, I.A., Tashiro, K. *et al.* Deciphering cytokine-driven ADP-ribosylation signaling networks via Af1521-based mass spectrometry analysis of labile Glu/Asp-linkages. *Nat Commun* (2026). https://doi.org/10.1038/s41467-026-73677-x

Sara C. Buch-Larsen, Ivo A. Hendriks, Kyuto Tashiro, Jonas D. Elsborg, Sergey Y. Vakhrushev, Jesper V. Olsen, Bernhard Lüscher, Glen Liszczak, Ivan Ahel & Michael L. Nielsen

Deciphering cytokine-driven ADP-ribosylation signaling networks via Af1521-based mass spectrometry analysis of labile Glu/Asp-linkages

Sara C. Buch-Larsen[1,2*#], Ivo A. Hendriks[1,2*#], Kyuto Tashiro[3], Jonas D. Elsborg[1,4], Sergey Y. Vakhrushev[2], Jesper V. Olsen[1,2], Bernhard Lüscher[5], Glen Liszczak[3], Ivan Ahel[4], and Michael L. Nielsen[1]

1 Proteomics program, Novo Nordisk Foundation Center for Protein Research, Department of Cellular and Molecular Medicine, Faculty of Health and Medical Sciences, University of Copenhagen, Copenhagen, Denmark
2 Copenhagen Center for Glycocalyx Research, Department of Cellular and Molecular Medicine, Faculty of Health Sciences, University of Copenhagen, Copenhagen, Denmark
3 Department of Biochemistry, University of Texas Southwestern Medical Center, Dallas, Texas, United States
4 Sir William Dunn School of Pathology, University of Oxford, Oxford OX1 3RE, United Kingdom
5 Institute of Biochemistry and Molecular Biology, RWTH Aachen University, Aachen, Germany

* These authors contributed equally to this work.
# Correspondence to: sara.larsen@cpr.ku.dk and ivo.hendriks@cpr.ku.dk

ABSTRACT

ADP-ribosylation (ADPr) is a regulatory post-translational modification targeting nine amino acid residues, but glutamate/aspartate-linked ADPr (Glu/Asp-ADPr) is labile and remains challenging to detect using conventional mass spectrometry (MS)-based workflows. Using synthetic peptides, we show that ester-linked Glu/Asp-ADPr is lost under alkaline conditions, elevated temperatures, and by hydrolysis via wildtype Af1521. We developed an acidic enrichment workflow incorporating an Af1521 mutant that preserves Glu/Asp-ADPr, enabling site-specific, system-wide MS analysis. In cytokine-stimulated A549 and HeLa cells, we identified >600 Glu/Asp- and >200 Cys-ADPr sites. Glu/Asp-ADPr marks cytoplasmic, immune-related protein networks, contrasting with nuclear Ser-ADPr. Quantitative profiling revealed reproducible, cell type- and treatment-specific patterns. PARP10-mediated Glu/Asp ADPr of ubiquitin indicates direct crosstalk with ubiquitin signaling pathways. Interferon treatments revealed conserved antiviral PARP networks extensively modified on Glu/Asp residues. Together, our work establishes a robust MS-based workflow and provides a resource of site-specific ADPr events, revealing residue-specific ADPr in innate immune signaling.

INTRODUCTION

ADP-ribosylation (ADPr) is an emerging post-translational modification (PTM) that plays a crucial role in diverse cellular processes, including DNA repair, transcriptional regulation, and immune signaling[1,2]. It is catalyzed primarily by PARP enzymes[3], which transfer ADP-ribose moieties from NAD^+ to the amino acid side chains of target proteins. Although ADPr was first described more than 60 years ago[4], many aspects remain poorly understood and are still under debate – including fundamental questions such as which amino acids serve as predominant targets under specific cellular conditions.

Recent advances in mass spectrometry (MS)-based proteomics have transformed PTM research by enabling unbiased, proteome-wide analyses[5]. However, ADPr presents unique analytical challenges that have hindered its comprehensive characterization. It is highly dynamic and transient, typically very low abundant, and structurally complex. ADPr can occur either as mono-ADPr, where a single ADP-ribose moiety is attached, or as poly-ADPr, in which ADPr chains are built upon pre-existing ADPr modifications[1,2]. Furthermore, it has been shown to modify at least nine different amino acid residues; Cys, Asp, Glu, His, Lys, Arg, Ser, Thr, and Tyr[6]. We have previously demonstrated that ADPr is exceptionally labile under higher-energy collisional dissociation (HCD) fragmentation, and thus for accurate site localization the non-ergodic fragmentation propensity of electron-transfer dissociation (ETD)-based approaches is required[6].

Over the past decades, several MS-based strategies have been developed to tackle these challenges, each with distinct advantages and limitations[7,8,9,10,11,12]. Some methods offer broad coverage but reduced specificity, while others achieve high confidence in site localization at the cost of sensitivity or enrichment efficiency. Consequently, these complementary approaches have collectively advanced the field but often capture only partially overlapping subsets of the ADPr landscape. A major breakthrough came with the identification of serine ADPr, particularly in the DNA damage response, mediated by PARP1 and PARP2 in concert with the cofactor HPF1[13,14,15,16]. Using Af1521 macrodomain-based enrichment strategies, we and others have developed MS workflows that robustly detect serine-linked ADPr, greatly expanding knowledge of its regulatory roles[6,10,12]. Despite this progress, other physiologically relevant ADPr linkages remain underexplored. In particular, glutamate- and aspartate-linked ADPr have proven especially challenging to study. It has recently become clear that these acidic residue linkages are highly labile under the mildly basic conditions (pH 8-8.5) routinely used in standard MS-based workflows for protein lysis and digestion[17]. This property likely explains their systematic underrepresentation in previous datasets and underscores the need for tailored analytical strategies to study these modifications.

Here, we present an MS-based workflow designed specifically for the detection of Glu- and Asp-linked ADPr. This strategy overcomes key technical limitations and enables confident site-specific identification of these modifications. Applying this approach, we performed in-depth and system-wide screens of Glu/Asp-linked ADPr in response to cytokine treatment, in both A549 cells and HeLa cells with induced PARP10 expression, uncovering insights into ADPr regulation in immune signaling and provide a rich resource for investigating residue-specific ADPr linkages in diverse biological contexts.

RESULTS

ADPr linkages differ markedly in stability across proteomics sample preparation conditions

Recently, the lability of ester-linked ADP-ribosylation was demonstrated in the context of alkaline or high-temperature conditions[17,18,19]. Over the last decade, we and others have performed multiple mass spectrometry (MS) screens with the routine usage of alkaline conditions and long incubations at room temperature or above during sample preparation[6,7,10,12,20], suggesting that ester-linked ADPr (i.e. Glu/Asp-ADPr) has been poorly conserved. Here, we set out to systematically assess the stability of ADPr linkages to four different amino acid residues, in the context of standard MS-based proteomics sample preparation conditions and buffers (Fig. 1A). For this purpose, we used synthetic peptides with a largely homologous sequence, with ADPr linked specifically to an Asp, Glu, Arg, or Ser residue. The peptide sequences were non-isobaric to allow distinguishing them easily even from mixtures, and all analysis was performed with the ETD-capable Lumos mass spectrometer to allow confident identification and localization of the ADPr within each peptide.

We first investigated the overall stability of the four different linkages over time, by incubating them for up to one week in a high-performance liquid chromatography (HPLC) system under standard proteomic sample conditions, i.e. in 0.1% formic acid in a 96-well plate kept at 7 °C (Fig. 1B). Reassuringly, we found that all four linkages are highly stable under these conditions, with at most ~5% degradation for Arg-ADPr over the course of one week, supporting that LC-MS conditions are not problematic for the analysis of any ADPr linkage type. Next, we incubated the peptide mixtures for three hours in buffers with varying pH (Fig. 1C), and confirmed the previously observed lability of Glu/Asp-ADPr at alkaline conditions. Notably, even under physiological conditions ester-linked ADPr is not entirely stable, and furthermore we also observed that half of Arg-ADPr was reversed under highly alkaline conditions that are typically employed during high-pH fractionation[12]. Acidifying the mixtures prior to vacuum concentrating them at 60 °C was only able to partially prevent hydrolysis of ADPr (Supplementary Fig. 1A). As a control, we also incubated

the ADPr peptide mixture using hydroxylamine, either pH-neutralized or not (Supplementary Fig. 1B). Indeed, hydroxylamine very rapidly reversed Glu/Asp-ADPr, whereas Ser-ADPr was unaffected. We found that Arg-ADPr was also affected by hydroxylamine, with ~25% loss after 15 min, ~50% loss after 3 h, and essentially total loss after 24 h.

Finally, we assessed the impact of the Af1521 macrodomain on ADPr stability, as Af1521 is routinely used for enrichment of ADPr, and has been reported to exhibit Glu/Asp-ADPr hydrolase activity[21,22]. We first evaluated the wildtype Af1521 under different buffer conditions, and found that it can remove Glu/Asp-ADPr, particularly at elevated pH and temperature (Fig. 1D). Notably, at pH 8.5 and 4 °C, conditions commonly used during proteomics sample preparation, Af1521 can readily reverse Glu/Asp-ADPr. To investigate whether this effect could be mitigated, we compared wildtype Af1521 with an engineered (K35E / Y145R) mutant[23,24], and incubated our synthetic ADPr peptide mixture with the macrodomains using various buffer conditions (Fig. 1E-F, Supplementary Figs. 1C-D). Under mildly acidic conditions (pH 6.3) and at 4 °C, both macrodomains largely preserved Glu/Asp-ADPr over several hours. However, upon increasing temperature or pH, hydrolysis of ester-linked ADPr was markedly accelerated in the presence of wildtype Af1521 (Fig. 1E), whereas a substantially higher amount (5- to 10-fold) of Glu/Asp-ADPr was retained when using the mutant Af1521 (Supplementary Fig. 1C).

To better mimic our Af1521 enrichment workflow, we performed pulldown experiments using the synthetic ADPr peptide mixture, followed by washing steps and bead elution (Fig. 1F). Here, we observed that the mutant Af1521 consistently recovered higher levels of Glu/Asp-ADPr compared to the wildtype protein, even under conditions (i.e. pH 6.3 and 4 °C) where overall hydrolysis was limited (Supplementary Fig. 1D). This difference became more pronounced under conditions that promote ADPr lability, with 10- to 30-fold higher recovery of Glu/Asp-ADPr using mutant Af1521 (Supplementary Figs. 1C-D). Importantly, Ser- and Arg-ADPr remained stable throughout these experiments, although the engineered Af1521 displayed slightly higher (1.5- to 2-fold) recovery of these linkage types following pulldown (Fig. 1F). While these experiments do not fully disentangle contributions from hydrolysis rate and binding efficiency, they demonstrate that both buffer conditions and macrodomain choice strongly influence the preservation and recovery of ester-linked ADPr.

Taken together, these findings highlight the pronounced sensitivity of Glu/Asp-linked ADPr to both chemical and enzymatic hydrolysis during sample preparation, and identify acidic conditions in combination with the mutant Af1521 macrodomain as a strategy to improve preservation of these labile modifications.

Acidic workflow and mutant Af1521 uncover hidden Glu/Asp-ADPr

Based on our observations using the synthetic ADPr peptides, we set forth to adapt and benchmark our Af1521 enrichment methodology, aiming to establish a MS-based strategy that can stably purify and identify the labile ester-linked Glu/Asp-ADPr (Fig. 2A). To this end, we utilized three distinct and relevant cellular systems that putatively encompass a wide range of different ADPr linkage types. These included interferon-treated A549 cells; where MAR is expected through PARP14 activation[25,26], H_2O_2-treated HeLa cells; where a large accumulation of Ser-ADPr is expected[6,15,27,28]; and H_2O_2-treated U2OS HPF1 knockout cells; wherein a shift towards Glu/Asp-ADPr is anticipated[15,29,30]. We either performed our established Af1521-based workflow[12], which relies on alkaline conditions, or otherwise we utilized our modified Af1521 workflow under acidic conditions . To facilitate direct comparison while preserving labile ADP-ribosylation, the acidic workflow was designed to closely mirror the established alkaline protocol, with the primary differences being reduced pH (<6.3 at all times) and shortened incubation times. A summary of key differences between the workflows is provided in Supplementary Data 1. Furthermore, we evaluated both approaches in the absence or presence of PARG, and utilized either wildtype or mutant (K35E / Y145R) Af1521 macrodomain[23,24] (Fig. 2B).

All samples were analyzed using ETD-based mass spectrometry and data was processed in an unrestricted manner where ADPr is theoretically allowed to reside on any of the twenty naturally occurring amino acid residues. Overall, we found that both the alkaline and acidic methods were comparably efficient at generating samples that facilitated MS-based localization of the ADPr moiety to specific amino acid residues (Supplementary Fig. 2A), with approximately two-thirds of peptide-spectrum-matches (PSMs) localized at a >90% probability. Furthermore, across all samples investigated, we were able to confidently detect (>99% localization) ADPr on the nine previously reported reactive amino acids[6], with no strong evidence for modification of any further residue types (Supplementary Fig. 2B). Thus, all further data analyses were performed with ADPr allowed to reside on Cys, Asp, Glu, His, Lys, Arg, Ser, Thr, and Tyr residues.

In the context of interferon-treated A549 cells, we were able to identify several hundreds of ADPr sites (Supplementary Data 1). Intriguingly, the distribution of linkage types varied dramatically depending on the purification strategy used, with Glu/Asp-ADPr exclusively detected using the acidic workflow (Fig. 2C and Supplementary Fig. 2C), and Glu as the main acceptor site. Notably, this was only observed when using the mutant Af1521, validating our experiments using synthetic peptides (Figs. 1E-F and Supplementary Figs. 1C-D), and demonstrating that the mutant Af1521 macrodomain is much more suitable for purification of labile ester-linked ADPr from complex samples. The combination of wildtype Af1521 and acidic conditions resulted in mainly unmodified background peptides being detected (Supplementary Fig. 2D), with ADPr peptide purity

at ~10% otherwise. Notably, Cys-ADPr was mainly observed when using the mutant Af1521, and prominently under alkaline conditions.

When considering H_2O_2-treated HeLa cells, we could readily reproduce the preponderant presence of Ser-ADPr, with just under 1,000 sites detected (Fig. 2D, Supplementary Fig. 2E and Supplementary Data 1). Regardless of the purification workflow, Ser-ADPr remained dominant especially by abundance, although interestingly the efficiency of Ser-ADPr purification was greatly diminished from the alkaline (~80% purity) to the acidic (~5-25% purity) workflow (Supplementary Fig. 2F). The mutant Af1521 was overall able to increase the total abundance of purified ADPr (Supplementary Fig. 2E), which paradoxically decreased the number of identified sites under alkaline conditions while increasing the number under acidic conditions (Fig. 2D).

In the absence of HPF1, the transfer of ADPr to Ser is greatly diminished[13,15,31]. Indeed, HPF1 knockout cells in response to H_2O_2 treatment, we observed a dramatic reduction in the number of Ser-ADPr sites and their overall abundance (Fig. 2E, Supplementary Fig. 2G and Supplementary Data 1), compared to a HPF1-proficient system (Fig. 2D and Supplementary Fig. 2E). Utilizing the mutant Af1521 and the alkaline workflow revealed the presence of additional ADPr, mostly targeting Cys and His residues. Moreover, the combination of the mutant Af1521 and the acidic workflow uncovered a considerable number of Glu/Asp-ADPr sites, representing ~90% of the overall ADP-ribosylome, hereby indicating a molecular switch from Ser to Glu/Asp targeting. Notably, this analysis was qualitative and different cellular backgrounds were used in the context of HPF1 presence. Interestingly, across all three cellular systems, we did not observe any notable effect of incubating the samples with PARG (Figs. 2C-E). Further, we noted that in all cellular contexts and while using the mutant Af1521, we could achieve a peptide purity of at least 10-20%, which is on par or superior to antibody-based enrichments[31].

Overall, we demonstrate that our strategy utilizing the Af1521 macrodomain and either alkaline or acidic conditions, can capture the heterogeneity of ADPr acceptor sites entailed within diverse biological systems.

Ser and Glu/Asp-ADPr target distinct biological and subcellular proteins

Across all conditions we investigated during the benchmark experiments (Fig. 2), we observed ADPr to most frequently target Ser, Glu/Asp, Arg, and Cys residues (Fig. 3A). Although the comparison was technical in nature with a focus on different lysis and purification conditions, and was performed from one sample batch, we nevertheless explored how the different ADPr linkage types correlated to their respective biological origins.

As anticipated, considering the cumulative number over all conditions, ADPr on serine residues was the most frequently observed (Fig. 3A), with the vast majority found in H_2O_2-treated

HeLa cells (Fig. 3B). In the absence of HPF1, or in A549 cells that were not treated with H_2O_2, Ser-ADPr only targeted a few proteins. In these cases, there was still a considerable overlap to Ser-ADPr detected in H_2O_2-treated HeLa. In case of Glu/Asp-ADPr, in contrast to Ser-ADPr, the majority of sites and target proteins were observed in IFN-treated A549 and H_2O_2-treated U2OS lacking HPF1 (Fig. 3C). Interestingly, despite similar numbers of Glu/Asp-ADPr sites identified in both of these systems, their overlap was relatively small at both the site and the protein level, hinting at distinct biological pathways being targeted. For Cys-ADPr, most detections occurred in IFN-treated A549, with only a few in the other two systems (Supplementary Fig. 3A). Interestingly, whereas for Glu/Asp-ADPr we found on average 3 sites-per-protein, for Cys-ADPr the majority of target proteins contained exactly one site. We noted Arg-ADPr to occur somewhat sporadically across the three cell lines, with an overall poor overlap (Supplementary Fig. 3B), which may be due to different expression levels of ARTC enzymes[32].

For the two largest groups of ADPr sites, Ser and Glu/Asp, we examined the annotated subcellular localization of their respective target proteins based on Gene Ontology annotations (Fig. 3D). As expected, we found that Ser-ADPr significantly targeted nuclear proteins across all biological systems investigated, consistent with writers of this modification localizing to the nucleus[33]. In case of H_2O_2 treatment in HPF1-proficient cells, chromatin-associated proteins were also a significant target. Intriguingly, in HPF1-deficient cells, the chromatin targeting significantly shifted to Glu/Asp-ADPr, suggesting that the same proteins or biological pathways may remain targeted by ADPr, but with altered amino acid specificity. Finally, considering IFN-treated A549, the Glu/Asp-ADPr uniquely and significantly targeted cytoplasmic proteins, demonstrating that certain linkage types can target different subcellular pathways or compartments depending on biological context.

Quantitative profiling reveals robust and reproducible Glu/Asp-ADPr landscapes

Having established a strategy able to judiciously identify glutamate- and aspartate-linked ADPr, we wanted to validate our approach in a quantitative manner. To this end, we set up a large-scale quadruplicate experiment wherein we compared untreated A549 cells with IFNα- or IFNγ-treated cells. Furthermore, we included HeLa cells which allow for selective expression of PARP10, which is a prominent Glu/Asp mono-ADPr transferase[34,35], and performed either mock, IFNα, or TNFα treatment (Fig. 4A). For enrichment of ADPr, we utilized our acidic workflow employing brief PARG incubation, mutant Af1521, and analyzed all samples using ETD-based mass spectrometry.

In total, we identified 906 high-confidence ADPr sites residing on 454 target proteins (Fig. 4B, Supplementary Data 2 and 3), with approximately two-thirds of proteins modified by a single ADPr (Supplementary Fig. 4). Only a small subset of ADPr sites was found in all conditions,

highlighting the biological variability between the conditions (Fig. 4B). We reproducibly identified between 200 and 400 ADPr sites per condition, with the higher numbers observed after cytokine treatment (Fig. 4C), although we observed a higher baseline ADPr abundance in HeLa cells (Fig. 4D). Overall, ADPr most frequently targeted Glu, Asp, Cys, and Ser residues, with the latter responsible for the higher baseline in HeLa compared to A549 cells (Fig. 4E, Supplementary Figs. 4B-C). Consistent with the targeting of ADPr to Glu/Asp in our benchmark experiment (Figs. 2-3), we found that modification in A549 cells primarily targeted Glu/Asp, especially following interferon treatment. When expressing PARP10 in HeLa cells, Glu-ADPr was prominently induced, in lieu of the Ser-ADPr that was otherwise notably present in HeLa cells. In all cases, Cys-ADPr represented ~20% of all sites, and ~5-10% of overall ADPr abundance. Taken together, our data reveal highly distinct patterns in which amino acid types are targeted by ADPr, with either widespread modification of numerous residues or focused modification of a few sites, depending not only on treatment condition, but moreover on the cellular system employed.

We observed an overall high degree of reproducibility, with average Pearson correlations of 0.91 to 0.96 within same-condition replicates (Supplementary Fig. 4D). As expected, correlation was lower across different treatment conditions within the same cell type, and much lower across different cell lines. Hierarchical clustering of the data further illustrated a high degree of same-condition replicate reproducibility (Fig. 5A), while visualizing distinct clusters of ADPr target proteins. Principle component analysis revealed that the primary degree of variance originates from the different cell lines, followed by untreated versus cytokine-treated, with only modest variance within treatment clusters (Fig. 5B).

To assess treatment-induced changes in the overall proteomic landscape, we performed a total proteome analysis by MS using input samples from the ADP-ribosylome experiments. In total, we identified 9,534 proteins (by unique gene name; i.e. protein-coding genes), of which 9,334 could be quantified in quadruplicate (Supplementary Data 4). Hierarchical clustering showed high similarity between same-condition replicates (Supplementary Fig. 5A), while the largest source of variation was observed between A549 and HeLa cells (Supplementary Fig. 5B). Compared to the ADP-ribosylome (Figs. 5A-B), variation in the total proteome was more strongly dominated by differences between cell lines, while cytokine-induced effects were comparatively subtle, indicating that ADP-ribosylation exhibits a more pronounced response to such perturbations than overall protein abundance. Notably, the vast majority (~97%) of ADPr target proteins was also detected in the total proteome (Supplementary Fig. 5C). However, linear regression analysis revealed only a weak correlation between protein abundance and ADPr levels for the same proteins (Supplementary Figs. 5D-E and Supplementary Data 4), suggesting that changes in the ADP-ribosylome are largely uncoupled from protein expression levels.

Since we developed a methodology capable of preserving labile Glu/Asp-linked ADPr, and profiled several hundreds of Glu/Asp-ADPr sites across both our benchmarking and quantitative experiment, we wanted to evaluate the comprehensiveness of our profiling. To this end, we compared all ADPr sites mapped in this work (Fig. 5C and Supplementary Data 5), to previous MS-based proteomics studies that facilitated Glu/Asp-ADPr identification[7,18,36,37]. Three of these studies relied on hydroxylamine-derivatization of Glu/Asp-ADPr prior to MS using collisional fragmentation[7,36,37], whereas the most recent study similarly to us relied on electron-based fragmentation of peptide bearing the intact ADPr moiety[18]. We first assessed the depth of sequencing achieved across these studies via comparison of known protein copy-numbers and correlating these to the identified ADPr target proteins (Fig. 5C). Overall, our experiments reached a similar depth of sequencing compared to the two studies from the Yu lab, and achieved greater depth than the other ADPr studies in the comparison (Supplementary Data 5). When considering overlaps in ADPr target proteins across studies, whereas there were some large groups of study-specific proteins, we overall see a very strong overlap between our work and the three studies with most ADPr identifications. Interestingly, at the site-specific level, our study overlaps best with the most recent, smaller study, which also relied on an acidic sample preparation workflow and ETD-based fragmentation (Fig. 5C). Taken together, we identified >600 high-confidence Glu/Asp-linked ADPr sites across conditions and cell types with strong reproducibility (Supplementary Data 1 and 2). Results showed cell line- and treatment-specific ADPr patterns, with robust protein-level overlap to previous studies, confirming both the depth and reliability of our profiling approach.

PARP10 rewires the ADP-Ribosylome and targets ubiquitin for ADPr

Expression of PARP10 in HeLa cells did not result in a difference in the overall number of ADPr sites identified, nor did the overall ADPr abundance change (Figs. 4C-D). However, based on the hierarchical clustering and principal component analysis, there was a considerable and consistent change in the overall ADP-ribosylome following PARP10 induction (Figs. 5A-B). Indeed, volcano plot analysis demonstrated a significant re-wiring, with 61 proteins upregulated and 47 proteins downregulated in their ADP-ribosylation (Fig. 6A). Overall, 47 (~77%) of the upregulated proteins were annotated as cytosolic, whereas 42 (~89%) of the downregulated proteins were annotated as nuclear (Supplementary Data 3). Reassuringly, PARP10 itself was found to be ADP-ribosylated upon expression. Further treatment of this cellular system with either IFNα or TNFα resulted in significant upregulation of 55 or 13 proteins (Fig. 6B and Supplementary Fig. 6A), respectively, with only five proteins downregulated in case of IFNα treatment. Altogether, while treatment with IFNα induced a robust effect with modification of the PARP9/PARP14/DTX3L axis[25,26,38], TNFα did not elicit a notable response within our experimental setup.

To assess the relationship between ADP-ribosylation and protein abundance, we compared changes in the ADP-ribosylome to those observed in the total proteome under the same conditions (Supplementary Figs. 6B-D). Despite substantial numbers of significantly regulated proteins in both datasets, the overlap was minimal. In the case of PARP10 expression, PARP10 itself was the only protein significantly regulated at both the ADPr and total proteome level (Supplementary Fig. 6B), whereas for IFNα and TNFα treatments only a small number of proteins overlapped (5 and 1, respectively) between the two analyses (Supplementary Figs. 6C-D). Consistently, correlation analyses revealed weak relationships between ADPr and protein abundance changes, and no significant enrichment of overlapping proteins was observed. Together, these findings indicate that changes in ADP-ribosylation occur largely independently of protein abundance, supporting the notion that the ADP-ribosylome captures a distinct regulatory layer.

PARP10 expression resulted in a considerable shift in the ADP-ribosylome, and within this context we investigated which proteins overall were the most highly modified by ADP-ribosylation (Fig. 6C). Intriguingly, within the top five most abundantly modified proteins, we noted that ubiquitin was prominently ADP-ribosylated in the presence of PARP10, with over 30-fold induction. Ubiquitin has previously been implicated in the context of PARP10, and is the only PARP enzyme to contain Ubiquitin Interaction Motifs[39]. Thus, we scrutinized the amino acid residues of ubiquitin that were direct targets of ADP-ribosylation, and ten ADPr sites could be quantified on ubiquitin in HeLa cells (Figs. 6D-E). Under standard growth conditions most (~77%) ADPr was observed at the ubiquitin C-terminus, either on Arg-74 or on the terminal carboxyl group, whereas expression of PARP10 led to ~86% of the total modification on E-51 (~57%), D-32 (~19%), and E-24 (~10%). From a structural point of view, these three residues are in close proximity and surface-accessible, located opposite from the di-glycine through which ubiquitin is conjugated (Fig. 6F). Alignment of ubiquitin sequences across species revealed that these Asp and Glu residues are essentially fully conserved from human all the way down to yeast (Supplementary Fig. 6E). In contrast, alignment of ubiquitin with all human ubiquitin-like proteins showed limited conservation of these acidic residues (Supplementary Fig. 6F), suggesting that PARP10-dependent ADP-ribosylation preferentially targets ubiquitin rather than other ubiquitin-like modifiers. With ADPr-Ub (also referred to as MARUbylation) recently discovered[40,41,42,43], we performed a re-analysis of our proteomics data, accommodating ADPr-ubiquitylation. Our enrichment strategy was not designed with ADPr-Ub in mind, but we nevertheless confidently identified one ADPr-Ub on E-24 of ubiquitin (Fig. 6G), exclusively in the presence of PARP10 in combination with IFNα treatment, suggesting that PARP10 may be involved in formation of mixed ubiquitin-ADPr-ubiquitin chains in the context of immune signaling.

Interferons drive extensive Glu/Asp/Cys-ADPr on immune-linked networks

A549 cells are commonly used to study immune signaling pathways[44,45,46]. We applied our Glu/Asp-ADPr compatible methodology to investigate the ADP-ribosylome in the context of interferon treatment of A549 cells (Fig. 4A). Treatment with either IFNα or IFNγ doubled the number of identified ADPr sites (Fig. 4C and Supplementary Data 2), while overall abundance increased by 5-fold (Fig. 4D). Volcano plot analysis revealed that upon IFNα and IFNγ treatment, 116 and 146 ADPr target proteins were upregulated, and 5 and 2 were downregulated, respectively (Supplementary Figs. 7A-B and Supplementary Data 3). Comparison of ADPr and total proteome ratios under the same conditions revealed limited overlap between the two layers, with the majority of regulated proteins being unique to either the ADP-ribosylome or the proteome (Supplementary Figs. 7C-D). Consistent with this, correlation analyses showed weak relationships between ADPr and protein abundance changes, and no significant enrichment of overlap was observed. The small subset of commonly regulated proteins included key interferon-responsive factors; PARP9, PARP12, PARP14, DTX3L, and NMI. Of note, both interferon treatments resulted in comparable subsets of proteins being regulated by ADP-ribosylation. Thus, we directly compared proteins modulated by ADPr in the IFNα and IFNγ experiments (Fig. 7A), which revealed 103 proteins that were significantly regulated by both interferons, and 66 proteins significantly regulated by only one IFN. Out of the 540 ADPr sites identified in A549 cells, 312 (58%) sites resided on the proteins that were regulated in response to both interferons. At the site level, we found that the vast majority of significantly interferon-regulated ADPr sites were either Glu, Asp, or Cys linkages (Fig. 7B). In contrast, Ser-ADPr, even though abundantly present in the samples, was mostly unaffected by interferon treatment.

Next, we explored the biological properties of the 102 proteins that were increasingly ADP-ribosylated in A549 cells, both in the case of IFNα and IFNγ treatment (Fig. 7C and Supplementary Data 3). Via network connectivity analysis using the STRING database[47], 96 out of 102 proteins formed one significantly ($p < 10^{-16}$) interconnected cluster, with ADPr on these proteins mainly targeting Glu, Asp, and Cys residues. Interestingly, modification of Cys tended to preclude modification of Glu/Asp, and vice versa. Furthermore, modification by Cys-ADPr seemed to only target one site per protein, whereas Glu/Asp-ADPr frequently targeted up to several dozen sites per protein, in line with observations during our benchmark experiments (Figs. 3A and Supplementary Fig. 3A). Within the interferon-regulated ADPr target network there was an overrepresentation of cytoplasmic proteins, and moreover there was a significant presence of proteins involved in immune regulation, infectious disease, and the cellular response to stress (Supplementary Data 6). Taken together, our work demonstrates that interferon treatment of A549

cells induces extensive Glu/Asp/Cys-specific ADP-ribosylation of a highly interconnected network of cytoplasmic proteins enriched for immune- and stress-related functions.

Interferons remodel a core antiviral PARP network through distinct ADPr patterns

We profiled the ADP-ribosylome of A549 cells, as well as HeLa cells expressing PARP10, both treated with various cytokines. Among the hundreds of ADPr target proteins we identified (Supplementary Data 3), we also found 10 PARP family members to be ADP-ribosylated; PARP1, PARP2, TNKS2, PARP7, PARP8, PARP9, PARP10, PARP12, PARP13, and PARP14 (Fig. 8A). Intriguingly, across two distinct cell lines, and two different interferon treatments, we observed a strong modification of PARP9, PARP12, PARP13, and PARP14. Interestingly, TNKS2 showed an inversed trend in A549 cells following interferon treatment. We also noted PARP10 induction resulting in increased ADP-ribosylation of PARP7 (Fig. 8A), and a stable baseline of PARP1, PARP2, and PARP8 in HeLa cells regardless of treatment.

Comparing the regulation of ADPr target proteins in response to IFNα between A549 cells and HeLa cells expressing PARP10 revealed that the majority of proteins (144; ~90%) was specifically regulated in either one of the cell lines (Fig. 8B). However, 15 proteins were significantly upregulated in both cell lines upon IFNα treatment (labeled in purple), hinting at a subset of ADPr target proteins that are canonically associated with the cellular immune response (Fig. 8C). Indeed, these proteins formed an interconnected network when clustering via the STRING database, with a sub-cluster including PARP9, PARP12, PARP13, PARP14, DTX3L, and TRIM25, all of which act as key regulators of antiviral and immune signaling pathways[48,49,50]. The network also extended into additional cellular processes: transcriptional and RNA regulation (CNOT1, ASCC3), vesicle trafficking (AP1G1), ribosomal translation (RPL18, RPS7), protein quality control (VCP), and cytoskeletal organization and dynamics (VIM, ANXA2, ACTN4).

Having established the interferon-regulated PARP network, we next examined the specific ADPr modification sites within the major antiviral PARPs to resolve how their regulation manifests at the residue level (Fig. 8D). Among the four antiviral PARPs, PARP14 showed the strongest ADP-ribosylation, with a total of 32 sites and predominant Glu/Asp modification. Across both HeLa and A549 cells, consistent ADPr modification was observed at E-856 and D-1216 in the PARP14 macrodomains, and at E-1562 and D-1604 in the WWE domain near the interface with the catalytic domain. The second-most modified antiviral PARP family member, PARP9, was modified on 16 sites. The majority of ADPr occurred on E-203, E-281, E-399, all residing in the macrodomains. The remaining two antiviral PARPs; PARP12 and PARP13, were not as heavily ADP-ribosylated, and interestingly both PARPs were predominantly modified on a single Cys residue, C-474 and C-721 respectively, located at the N-terminus of their catalytic domains.

In contrast to the antiviral PARPs, the other PARP family members displayed different site preferences. As anticipated, despite PARP1 modification occurring on a multitude of Glu/Asp residues, the vast majority of intensity (~99% in HeLa and ~96% in A549) was observed on Ser residues (Supplementary Fig. 8). Reassuringly, the Glu/Asp ADPr sites we detected here in PARP1 overlap well with the Glu/Asp sites reported by the Matic lab[18], and in both cases the ADPr resided in the auto-modification domain and towards the C-terminus of the second zinc finger domain. Expectedly, PARP2 ADPr exclusively occurred on a Ser residue. For the remaining four PARP family members, TNKS2, PARP7, PARP8, and PARP10, we were only able to detect between one and three ADPr sites, and interestingly in all cases >75% of modification occurred on Cys residues.

Taken together, our findings highlight a distinct subset of antiviral PARPs and associated proteins that are consistently ADP-ribosylated across cell types in response to interferon treatment, forming a core immune-regulated network. Moreover, our site-specific profiling of ADPr sites reveals distinct modification patterns across PARP family members and other immune system proteins, and represents a valuable resource for the field.

DISCUSSION

In this work, we augmented our established Af1521 proteomics enrichment workflow to profile glutamate- and aspartate-linked ADP-ribosylation, and applied it to cytokine-stimulated A549 and HeLa cells expressing PARP10. We profiled >600 Glu/Asp-ADPr sites across diverse cellular contexts, revealing extensive cell type- and treatment-specific ADPr patterns, but also uncovering a conserved interferon-induced network centered on antiviral PARPs and immune regulators. Consistent with this, comparisons to total proteome measurements across conditions revealed only limited overlap and weak correlation with ADP-ribosylation changes, indicating that the ADP-ribosylome largely represents a distinct regulatory layer rather than reflecting protein abundance.

The lability of ester-linked Glu/Asp-ADPr has recently been established[17,18,19], with the main drivers of lability being alkaline sample preparation conditions along with elevated temperatures and extended incubation times. Previously, our lab performed a range of MS-based proteomics studies wherein the Af1521 methodology was applied using alkaline conditions[6,31], and similarly other labs also predominantly use conditions that are incompatible with Glu/Asp-ADPr preservation[7,10]. Thus, we and others may have underestimated the prevalence of Glu/Asp-ADPr in the past, which should be taken into account when assessing previous datasets. However, the context of the experiments remains important, as the majority of our studies revolved around induction of DNA damage via treatment with oxidizing or alkylating agents[6,12,51], which primarily

trigger a robust Ser-ADPr response which is accurately visualized using Af1521 under both alkaline and acidic conditions (Fig. 2). Importantly, it should also be mentioned that a relevant biological system and context is required for studying Glu/Asp-ADPr, as this linkage type usually requires activation of a specific subset of writer enzymes[1], or otherwise has mainly been observed in HPF1-deficient cell systems[13,18,52].

Another relevant aspect to consider is the hydrolase activity of Af1521 itself[21,22]. Although there is some irony in using an active eraser enzyme to purify its target modification, we have demonstrated in the past that Af1521 is exceedingly efficient in enriching the majority of ADPr linkage types[12], and within the systems investigated we found no evidence of Af1521 reversing ADPr during the purification[53]. However, the hydrolase activity of Af1521 targeting Glu/Asp-ADPr, along with alkaline conditions employed during the ADPr enrichment procedure, could surely result in abolishment of Glu/Asp-linked ADPr during sample preparation. In this work, we circumvent the reversal of Glu/Asp-ADPr by using acidic conditions, lower temperatures, and shorter incubation times. Moreover, we found that, compared to wildtype Af1521, the mutant Af1521 substantially improves the recovery of Glu/Asp-ADPr, particularly under conditions where these linkages are otherwise prone to hydrolysis. Our data do not allow us to fully disentangle the relative contributions of reduced hydrolase activity and altered binding affinity. However, contribution from increased binding affinity appears comparatively modest, with only small increases observed for recovery of the otherwise stable Arg- and Ser-linked ADPr peptides (Fig. 1F). In contrast, the magnitude of the observed stability of Glu/Asp-ADPr in the presence of mutant Af1521 compared to wildtype Af1521 suggests that hydrolysis is likely the dominant factor (Fig. 1E and Supplementary Figs. 1C-D). This effect may be particularly pronounced in pulldown settings (Fig. 1F and Supplementary Fig. 1D), where excess substrate is removed during washing steps, which in turn could amplify hydrolytic loss.

During our initial experiments using synthetic ADPr peptides, we observed a notable lability of Arg-ADPr under alkaline conditions at high temperature, as well as upon hydroxylamine treatment (Fig. 1C and Supplementary Fig. 1B). Arg-ADPr involves an N-glycosidic linkage at the ribose anomeric carbon, which is less stable than the O-glycosidic linkage of Ser-ADPr. This is consistent with its tendency for spontaneous anomerization[17,54], and the labile nature of Arg-ADPr under high temperature and high pH conditions[17]. Hydroxylamine is a strong nucleophile capable of reacting with electrophilic carbon centers such as the ribose anomeric carbon, and we speculate that nucleophilic attack on ADP-ribose may contribute to destabilization and hydrolysis of the Arg-ADPr bond. Further, lability of Arg-ADPr in response to hydroxylamine, even at neutral pH, has been described previously[55,56]. Together, this suggests that hydroxylamine treatment, commonly used to interrogate Glu/Asp-ADPr, may also partially affect Arg-ADPr under certain conditions.

We observed a notable number of Cys-ADPr sites across our experiments. Specifically, in the benchmarking experiment (Fig. 2), Cys-ADPr was observed predominantly when using the mutant Af1521 to enrich ADPr, and with a preference for alkaline conditions. Since Cys-ADPr has been reported to occur enzymatically and non-enzymatically[57], it could be speculated that under alkaline conditions Glu/Asp-ADPr may non-enzymatically transfer to Cys residues. To directly test this possibility, we performed experiments using *in vitro* auto-modified PARP1, which in the absence of HPF1 is modified almost exclusively on Asp and Glu residues. Incubation of auto-modified PARP1 under the full range of lysis and digestion conditions used in our workflow, including acidic or alkaline buffers, prolonged incubation, and the presence or absence of thiol alkylation, did not result in detectable ADP-ribosylation of Cys residues (Supplementary Fig. 9 and Supplementary Data 7). These results argue against substantial non-enzymatic transfer of ADPr from Glu/Asp to Cys under the conditions used in our ADP-ribosylome workflow. Furthermore, when comparing A549 cells treated with interferon and U2OS HPF1 knockout cells treated with H_2O_2, we found a notably different ratio between Glu/Asp and Cys-ADPr observed under acidic and alkaline conditions, whereas a similar ratio would be expected in case of non-enzymatic transfer. Finally, we investigated the sequence context of ADP-ribosylated and unmodified Cys residues, and found no significant difference (p = 0.36) between proximal (±7 aa) occurrences of Glu/Asp residues, with on average 1.75 Glu/Asp residues nearby 209 Cys-ADPr sites, and on average 1.83 Glu/Asp residues nearby 2,540 unmodified Cys residues from the same proteins (Supplementary Data 8). Thus, based on these *in vitro* experiments and two distinct observations, the Cys-ADPr we mapped likely has a biological origin. Furthering this, we observed Cys-ADPr to be the predominant (>2/3rd) modification on 119 proteins (Supplementary Data 3), including PARP7/8/10/12/13, TNKS2 and TNKS1BP1, as well as RNF166 which has been reported to control TNKS stability[58]. Additionally, 43 of the Cys-ADPr target proteins are annotated to have RNA binding properties (Supplementary Data 3), which corroborates a previous proteome-wide analysis that demonstrated PARP7 catalyzing Cys-ADPr, with many of its targets involved in RNA binding and other RNA regulatory roles[59]. Collectively, these findings support Cys-ADPr as a biologically relevant modification with potential roles in RNA regulation and protein stability.

Glu/Asp-ADPr has historically been profiled using hydroxylamine derivatization of the ADPr moiety, typically following boronate affinity enrichment[7,36,37]. Recently, the Matic lab published an antibody-based strategy for ADPr enrichment, wherein they also employed acidic conditions to stabilize Glu/Asp-ADPr[18]. Based on our comparison of ADPr sites and target proteins across all studies, we found that we best overlapped with the larger hydroxylamine studies at the target protein level, whereas at the site-specific level the highest agreement was with the recent study from the Matic lab (Fig. 5C). We reason that the protein-level overlap could align with the

overall number of ADPr target proteins identified, with the overlaps correlating with the size of the studies. At the site-specific level, both technical and biological factors are likely to play a role. First, we detect the full ADPr moiety using ETD-based fragmentation similar to the Matic lab, whereas other studies detect a hydroxylamine derivative using HCD-based fragmentation. Second, whereas the hydroxylamine-based method exclusively detects Glu/Asp-ADPr, the approach presented in this work is capable of detecting any ADPr linkage type. Third, in this study we employed acidic conditions during sample preparation, whereas in the hydroxylamine studies the samples are often first processed under alkaline conditions, which could result in some loss of Glu/Asp-ADPr prior to its reaction with hydroxylamine. Fourth, the Matic lab investigated Glu/Asp-ADPr in the absence of HPF1 to increase the cellular levels of Glu/Asp-ADPr[15], which aligns with our benchmark experiment, and generated the largest overlap, likely due to similarity of the biological context studied. Overall, considering the promiscuity of ADPr and its plethora of biological functions, and further convolution by differences in technical methodology, a large degree of heterogeneity is to be expected across different studies.

Our results reveal that PARP10 expression in HeLa cells does not increase the number of ADPr sites, nor the overall abundance of ADP-ribosylation (Figs. 4C-D), even though PARP10 protein levels were approximately 60-fold increased upon induction (Supplementary Data 4). An increase in ADP-ribosylation could be mitigated by the activity of ADPr hydrolases[60,61], however, we did not find any known ADPr hydrolases to be differentially expressed upon induction of PARP10 or cytokine treatment (Supplementary Data 4), although from total proteome data we cannot determine the activity of the ADPr hydrolases. ADP-ribosylation of ubiquitin has been reported and may influence ubiquitin signaling and proteasome-dependent turnover pathways[62,63]. In this context, ADPr within the ubiquitin system could potentially promote degradation of ADP-ribosylated substrates, providing an additional mechanism by which increased PARP10 activity might be buffered without leading to a detectable increase in overall ADPr abundance.

Nonetheless, PARP10 expression induces a profound rewiring of the ADP-ribosylome, shifting modification patterns from nuclear toward cytosolic proteins, in line with the cytoplasmic localization and signaling roles of PARP10 described previously[64]. Prior to PARP10 expression, we identify ubiquitin as a prominent ADPr target protein, with modification mainly occurring on Arg-74 or the terminal carboxyl group of the canonical di-glycine conjugation site. Our MS dataset does not provide enough direct spectral fragment evidence to distinguish between the two localizations, and further experiments would be necessary to discern between these two possibilities. Notably, PARP9/DTX3L was previously found to drive ADPr to the C-terminus of ubiquitin[65]. In line with this, we find DTX3L to become less ADP-ribosylated upon PARP10 expression, along with a shift from modification near the C-terminus of ubiquitin to multiple acidic residues that cluster in a structurally

accessible region opposite the di-glycine, suggesting that DTX3L modulates ubiquitin ADPr under baseline conditions.

ADP-ribose can additionally be directly modified by ubiquitin (ADPr-Ub, or MARUb)[66], which can target both proteins and nucleic acids and was first described to occur via DELTEX E3 ligases[67]. Interestingly, while ADPr on the C-terminus of ubiquitin was previously reported[65], it is possible that instead they observed ubiquitylation of ADPr. Similarly, in our MS proteomics data, we cannot rule out that what we observe is ubiquitylation of ADPr, rather than ADP-ribosylation of the ubiquitin C-terminal peptide. Otherwise, recombinant DTX2 is particularly able to ubiquitylate ADPr on auto-modified PARP10[40]. Another recent study also links PARP10 to ubiquitin signaling, where they found PARP10 and PARP7 to be substrates for ADPr-Ub in cells, referred to as MARUbylation[41]. They further find this MARUbylation was extended as K11-linked ubiquitin chains, which is likely mediated by the RNF114 E3 ligase and its paralogs[68,69]. Our data suggest that ubiquitin is not only a downstream target of PARP10-dependent ADPr, but ubiquitin may also be ADPr-ubiquitylated in the presence of interferon signaling, leading to mixed architecture chains (i.e. Ub-ADPr-Ub or Ub-MAR-Ub). We observed this with IFNα signaling, whereas Bejan et al. found MARUbylation modulated by IFNβ treatment, suggesting that this occurs consistently in the type-I interferon response, although Bejan et al. did not propose mixed architecture chains[41]. Together, these findings place PARP10 at the interface of ADPr and ubiquitin signaling, raising the possibility that ADPr-ubiquitylation of ubiquitin may contribute to the assembly of mixed ubiquitin-ADPr chains. However, additional biological follow-up studies will be necessary to further elucidate the potential regulatory functions of PARP10 in cellular signaling and immune responses.

Recent studies have increasingly linked ADP-ribosylation to innate immune and interferon signaling pathways, including roles for interferon-induced PARPs and ADPr dynamics in antiviral responses and inflammatory signaling[70,71,72,73]. Our findings complement these studies by providing a workflow that enables sensitive ETD-based detection of labile D/E-linked ADP-ribosylation, which may facilitate further investigation of these modifications in immune signaling contexts. IFNα and IFNγ regulate distinct and overlapping sets of proteins[74], and we found that in A549 cells the ADP-ribosylome was similarly modulated by both interferons, in either case triggering an extensive remodeling of the ADP-ribosylome, with a roughly twofold increase in the number of identified sites and a fivefold increase in overall ADPr abundance. At the site-specific level, we observed that the interferon-regulated ADPr was dominated by Glu, Asp, and Cys linkages, whereas Ser-ADPr remained largely unaffected, suggesting a preferential engagement of Glu/Asp/Cys-ADPr in interferon-responsive pathways. Network analysis revealed that the majority of interferon-regulated ADPr targets formed a highly interconnected cluster of cytoplasmic proteins enriched for immune, antiviral, and stress-related functions. Within this network, we identified a prominent axis of antiviral

PARPs and associated factors, including PARP9, PARP14, and DTX3L, with additional contributions from PARP12, PARP13, and TRIM25. Interferon treatment is known to activate PARP14, which then becomes the main driver of mono-ADPr in response, with PARP9/DTX3L regulating the activity of PARP14[25,26]. Consistently, in our data, these three proteins are the most abundantly ADP-ribosylated, with dozens of Glu/Asp modification sites. Immunoprecipitation of p62 from IFNγ-treated cells followed by mass spectrometry revealed interaction with and regulation of PARP14, PARP9, and DTX3L[75], along with several dozen other proteins for which we mapped ADPr sites in our screen. Although it is not clear from our data which PARPs target the aforementioned proteins, it is known that PARP14 targets p62, PARP13, RNF114, and RNF166[38]. Altogether, the coordinated ADPr of these proteins highlights a conserved, interferon-responsive module that may act as a central hub for antiviral signaling, linking residue-specific ADPr modifications to functional regulation of the innate immune response.

In conclusion, our work highlights the relevance of tailoring mass spectrometry-based workflows to the specific chemistry of ADP-ribosylation. As demonstrated here, subtle differences in buffer conditions, temperature, incubation times, and enrichment reagents during sample preparation can strongly influence the detection and quantification of labile ADP-ribosylation linkages, particularly on Glu/Asp residues. No single method is universally optimal, and differences in sample preparation and fragmentation strategies likely contribute to the heterogeneity observed across studies. Using an optimized acidic workflow with a mutant Af1521 macrodomain and ETD-based fragmentation, we achieved deep, site-specific coverage of Glu/Asp-ADPr across multiple cellular contexts and cytokine treatments. This dataset provides a rich resource for functional studies or mutagenesis, highlights both the context-specific nature of ADP-ribosylation and conserved networks such as the interferon-responsive antiviral PARP axis, while serving as a methodological reference for future ADPr profiling.

METHODS

Cell lines and cell culture

HeLa cells (CCL-2, female) and A549 cells (CCL-185, male) were acquired via the American Type Culture Collection (ATCC). U2OS cells (female) with HPF1 knockout (ΔHPF1)[33] and HeLa cells (female) with inducible PARP10 expression[76], were described previously. All cells were cultured at 37 °C and 5% CO2 in Dulbecco's Modified Eagle's Medium (Invitrogen) supplemented with 10% fetal bovine serum and a penicillin/streptomycin mixture (100 U/mL; Gibco). All cells were routinely tested for mycoplasma. Cells were not routinely authenticated.

Cell treatment

For induction of ADP-ribosylation in HeLa cells and U2OS ΔHPF1 cells, treatment was performed with 1 mM H_2O_2 (Sigma Aldrich) for 10 min or 30 min, respectively. For induction of ADPr signaling in A549 cells, treatment was performed for 24 h with either 0.684 ng/mL (~180 U/mL) IFNα (Peprotech) or 100 ng/mL (~194 U/mL) IFNγ (Peprotech). To express PARP10 in inducible HeLa cells[76], 1 µg/mL doxycycline was added for 24 h. Concomitantly, ADPr signaling was induced in the cells via addition of 0.684 ng/mL (~180 U/mL) IFNα (Peprotech) for 24 h, or addition of 5 ng/mL (~196 U/mL) TNFα (Peprotech) during the last 6 h. Approximately 200 million cells (~3 confluent square 25-cm dishes) were cultured per replicate. For downstream processing and MS analysis, replicate batches were divided over multiple purification conditions and technical replicates.

Cell lysis and protein digestion

For analysis of ADPr at alkaline pH, the full procedure for proteolytic digestion of cells was performed as described previously [6,12], and also detailed below. For purification of ADPr at acidic pH, the protocol was adapted considerably, with all changes outlined here. Cells were washed once with ice-cold PBS, and gently scraped at 4 °C in a minimal volume of PBS. For benchmarking experiments, all cell batches were divided equally between two tubes prior to lysis in different buffers. For quantitative experiments, all replicates were subjected to the acidic workflow. Cells were pelleted by centrifugation at 500*g*, and either lysed in 10 pellet volumes of Alkaline Lysis Buffer (6 M guanidine-HCl, 50 mM Tris-HCl, pH 8.5), or 10 pellet volumes of Acidic Lysis Buffer (6 M guanidine-HCl, 10 mM Tris-HCl, 100 mM sodium phosphate, pH 6.3). Complete lysis was achieved by alternating vigorous shaking with vigorous vortexing, for 30 seconds, prior to snap freezing of the lysates using liquid nitrogen. Frozen lysates were stored at −80 °C until further processing. Lysates were thawed and sonicated at 30 W, for 1 second per 1 mL of lysate, spread across 2 separate pulses. For acidic samples, care was taken to keep the lysates below 30 °C. Tris(2-carboxyethyl)phosphine and chloroacetamide were added to final concentrations of 10 mM. For alkaline samples, proteins were digested using Lysyl Endopeptidase (Lys-C, 1:200 w/w; Wako Chemicals) for 3 hours at 25 °C. For acidic samples in the benchmark experiment, proteins were digested using Lys-C (1:100 w/w) for 1 hour at 25 °C. For acidic samples in the quantitative experiment, lysates were first diluted to a final concentration of 3 M guanidine-HCl by addition of 100 mM sodium phosphate pH 6.3, prior to digestion using Lys-C (1:150 w/w) for 1 hour at 25 °C. Following Lys-C digestion, alkaline samples were diluted to a final concentration of 1.5 M guanidine-HCl using 50 mM Tris-HCl pH 8.5, and acidic samples were diluted to a final concentration of 1.5 M guanidine-HCl using 100 mM sodium phosphate pH 6.3. Alkaline samples

were further digested overnight using modified sequencing grade Trypsin (1:200 w/w; Sigma Aldrich). Acidic samples were further digested using sequencing grade Trypsin (1:150 w/w) for 1 hour at 25 °C. We note that trypsin activity is strongly inhibited by the presence of guanidine-HCl, and further slowed at pH 6.3. Trypsin could potentially be omitted from the workflow to pursue a Lys-C-only digest, which may still be compatible with identification of ADPr sites[12]. Following digestion, samples were (further) acidified by addition of trifluoroacetic acid (TFA) to a final concentration of 0.5% (v/v), cleared by centrifugation, and purified using reversed-phase C18 cartridges (Sep-Pak C18 6 cc Vac Cartridge, 500 mg Sorbent, Waters) according to the manufacturer's instructions, and using one cartridge per 20 mg of input protein. Elution of peptides was performed with 35% acetonitrile (ACN) in 0.1% TFA, peptides were frozen overnight at −80 °C, and afterwards lyophilized for 96 h.

Purification of Af1521 Macrodomain

GST- or His10-tagged Af1521 and Af1521-K35E/Y145R[23] macrodomains were produced in-house using BL21(DE3) bacteria, and coupled to glutathione Sepharose 4B beads (Sigma-Aldrich) or Ni-NTA Agarose beads (QIAGEN), respectively. Bacterial production of Af1521 and plasmids were described previously[6,12], and also detailed below. Competent BL21(DE3) were incubated with plasmid for 30 min, after which they were heat shocked at 37 °C for 2 min, incubated on ice for 2 min, allowed to recover for 1 h, plated on kanamycin LB plates, and incubated overnight at 37 °C. Four colonies were picked and transferred into LB media, growing overnight at 37 °C while shaking. The starter culture was diluted 1:20 and grown to a 600-nm optical density of 0.60, after which protein expression was induced through addition of IPTG to a final concentration of 0.5 mm for 5 h at 30 °C. Bacteria were collected by centrifugation, washed twice with PBS, and ultimately 100 ml worth of bacteria-containing LB was centrifuged per 50 ml tube. Bacterial pellets were frozen at −80 °C until further processing. Bacteria were lysed using BugBuster® Protein Extraction Reagent (Merck) according to the manufacturer's instructions, although for His10-tagged Af1521 an EDTA-free Protease Inhibitor Cocktail (Sigma-Aldrich) was used. His-tagged Af1521 was purified using Ni-NTA Agarose beads. GST-tagged Af1521 was purified from bacterial lysates using glutathione Sepharose 4B beads. 2.5 ml of beads (dry volume) were incubated with the bacterial lysate for 4 h at 4 °C in a head-over-tail mixer, after which they were washed five times using PBS. Tubes were changed after the second and fourth wash steps to minimize contaminant carryover, and pelleting of beads was performed in a swing-out centrifuge with delayed deceleration to minimize loss of beads, at 4 °C for 3 min at 500 × g. After the final wash, 1 ml of beads were stored per 15 ml tube, with PBS entirely filling up the tube, and supplemented with 10

mm sodium azide to retard microbial growth. Beads were stored at 4 °C until use, for up to three months.

Purification of ADP-ribosylated peptides using Af1521

Lyophilized peptides were dissolved in either Alkaline AP buffer (50 mM Tris-HCl, 1 mM $MgCl_2$, 250 µM DTT, and 50 mM NaCl, pH 8.0) or Acidic AP buffer (10 mM Tris-HCl, 100 mM sodium phosphate, 1 mM $MgCl_2$, 250 µM DTT, and 50 mM NaCl, pH 6.3). Dissolved peptides were cleared by centrifugation and supernatant decanted into clean tubes. For total proteome analysis by MS, a small portion of peptides was further digested with sequencing grade Trypsin (1:200 w/w; Sigma Aldrich) for 1 h at room temperature in 50 mM Tris-HCl, pH 8.5, prior to StageTip clean-up (detailed below). Subsequently, peptides were either left untreated or treated with PARG enzyme (kind gift from Prof. Dr. Michael O. Hottiger), with PARG added in a 1:1,000 (w/w) ratio for 1 h at room temperature. Beads were pre-washed twice with either Alkaline IP buffer (for alkaline samples) or Acidic IP buffer (for acidic samples). For benchmarking experiments, Sepharose beads with GST-tagged Af1521 or Af1521-K35E/Y145R were used for alkaline samples, whereas Agarose beads with His10-tagged Af1521 or Af1521-K35E/Y145R were used for acidic samples. For quantitative experiments, the (acidic) samples were briefly PARG-treated (1:1,000 w/w for 1 h at RT) and split equally, prior to purification of ADPr-modified peptides using either His10- or GST-tagged Af1521-K35E/Y145R. In all cases, peptides were chilled to 4 °C prior to addition of beads with Af1521, and otherwise kept on ice or inside a cold room (4 °C) at all points during the purification. The bead mixture was allowed to incubate on a rotating mixer at 4 °C for 45 min. For alkaline samples, beads were sequentially washed two times with ice-cold Alkaline AP Buffer, two times with ice-cold PBS, and two times with ice-cold MQ water. For acidic samples, beads were sequentially washed four times with ice-cold Acidic AP Buffer. On the first wash, beads were transferred to 1.5 mL protein-LoBind tubes (Eppendorf), and LoBind tubes were exclusively used from this point on to minimize loss of peptide. Following the third wash, beads were transferred to a fresh LoBind tube. For samples during the benchmarking experiments, ADP-ribosylated peptides were eluted from the beads using two elution steps of 15 min each, with two bead volumes ice-cold 0.15% TFA, and the pooled elutions were cleared through 0.45 µm spin filters (Ultrafree-MC, Millipore) and subsequently through pre-washed 100 kDa cut-off filters (Vivacon 500, Sartorius). For acidic samples during the benchmarking experiments, ADP-ribosylated peptides were additionally passed through pre-washed 10 kDa cut-off filters (Vivacon 500, Sartorius). For acidic samples during the quantitative experiments, half of the samples were purified using His10-Af1521-K35E/Y145R, with the other half purified using GST-Af1521-K35E/Y145R. Elution from the His10 Agarose beads was performed using two steps of 15 min each, using two bead volumes ice-

cold 0.15% TFA, with the pooled elutions passed through 0.45 µm, 100 kDa, and 10 kDa filters as described above. The cleared elutions were split in two halves, of which one set of halves were left as is, whereas the other set of halves were pH-neutralized via addition of 10 volumes of ice-cold 200 mM sodium phosphate pH 6.3, and cleared from histidine-rich background binders via a 15 min incubation with empty Ni-NTA beads, prior to re-acidification by addition of TFA to a final concentration of 1%. Elution from GST Agarose beads was performed firstly using two steps of 15 min each, with two bead volumes of ice-cold 0.1% formic acid (FA), and secondly for 15 min using four bead volumes of ice-cold 0.15% TFA. The FA and TFA elutions were kept separately, and both passed through 0.45 µm and 100 kDa filters as described above. After filtering, the FA elution was further acidified by addition of TFA to a final concentration of 0.15%.

StageTip purification of peptides

The filtered ADP-ribosylated peptides were purified using C18 StageTips at low pH. To this end, C18 StageTips were prepared in-house, by layering four plugs of C18 material (Sigma-Aldrich, Empore SPE Disks, C18, 47 mm) per StageTip. Activation of StageTips was performed with 100 µL 100% methanol, followed by equilibration using 100 µL 80% ACN in 0.1% FA, and two washes with 100 µL 0.1% FA. Samples that were not already acidic (pH < 3) were acidified via addition of TFA to a final concentration of 1%. Samples were centrifuged for 5 min at 14,000g, after which supernatants were loaded on StageTips. Subsequently, StageTips were washed twice using 100 µL 0.1% FA, after which peptides were eluted using 80 µL 30% ACN in 0.1% formic acid. All samples were dried to completion using a SpeedVac at 60 °C. Dried peptides were dissolved in 20 µL 0.1% FA and stored at −20 °C until MS analysis.

Peptide synthesis

Peptides containing site-specific ADP-ribosylation (ADPr) on defined residues were generated using a chemoenzymatic strategy. Peptides were synthesized by solid-phase peptide synthesis using standard Fmoc chemistry on Rink amide resin, purified by reversed-phase HPLC, and confirmed by LC–MS. Sequence variants were designed to enable ADPr installation on Arg, Ser, Glu, or Asp residues while maintaining comparable physicochemical properties. ADPr was enzymatically installed using recombinant ADP-ribosyltransferases under defined conditions: ARTC2.2 for Arg-ADPr, PARP1/HPF1 for Ser-ADPr, and the catalytic domain of PARP14 for Glu/Asp-ADPr, in the presence of NAD^+. Reactions were performed in buffered solutions at controlled temperature, quenched, and modified peptides were purified by reversed-phase HPLC and verified by LC–MS. Protocols and reagents for peptide synthesis, ADPr installation, and purification follow established chemoenzymatic approaches[17,77,77].

The following peptides were synthesized:
NH2-GWTARKSAEAGTAGK-amidated, either unmodified or with ADPr on Arg-5
NH2-GWTARKSAAAGTAGK-amidated, either unmodified or with ADPr on Ser-7
NH2-GWTARKAAEAGTAGK-amidated, either unmodified or with ADPr on Glu-9
NH2-GWTARKAADAGTAGK-amidated, either unmodified or with ADPr on Asp-9

Peptide sequences were chosen to have favorable properties for electron-transfer dissociation-based fragmentation, via inclusion of several arginine and lysine residues to ensure a suitable charge state during positive mode mass spectrometric analysis. Peptide sequences were otherwise kept as similar as possible to reduce bias, but nonetheless were not fully isobaric so that peptides may easily be distinguished from a mixture.

Synthetic peptide treatment

All lyophilized peptides were dissolved in 0.1% FA, and investigated using mass spectrometry for their overall ionization efficiencies (i.e. perceived signal by the mass spectrometer). A mixture with comparable amounts of all four ADP-ribosylated peptides was generated based on these observations, and used for all experiments. The synthetic ADPr peptide mixture was treated in various ways, as outlined in the figure legends. The “control” condition for all experiments corresponds to an otherwise untreated ADPr peptide mixture. Treatment at different pH utilized the following buffers. For “pH 3”, 0.1% formic acid. For “pH 5”, sodium acetate and acidic acid mixture calibrated to pH 5.0. For “pH 6.3”, 100 mM sodium phosphate calibrated to pH 6.3. For “pH 7.2”, phosphate buffered saline pH 7.2. For “pH 8.5”, Tris-HCl calibrated to pH 8.5. For “pH 11”, 50 mM ammonium hydroxide. Incubation with Af1521 macrodomain (either wildtype or mutant) was performed with GST-Af1521 coupled to beads. For pulldown experiments, the beads were washed four times with the same buffer as used during incubation. For non-control conditions from the experiments described in Figure 1C, 1D, 1E, and S1A-F, and following their treatments and pulldowns, all peptide mixtures were acidified using 1% TFA (v/v). Peptide-bead mixtures (e.g. following pulldown) were cleared through 0.45 µm spin filters (Ultrafree-MC, Millipore) and subsequently through pre-washed 100 kDa cut-off filters (Vivacon 500, Sartorius). All final samples were purified using C18 StageTip as described above.

In vitro PARP1 auto-modification

Full-length recombinant human PARP1 or PARP1 E988K were used for *in vitro* reactions. For each reaction, 10 µg of PARP1 was added to ~94 µL of auto-modification buffer (20 mM Tris-HCl, 50

mM NaCl, 5 mM $MgCl_2$, 0.1 mM TCEP, pH 7.5). To activate PARP1, 4 µL of 5 µM annealed oligos (5′ GGGTTGCGGCCGCTTGGG 3′ and 3′ CCCAACGCCGGCGGAACCC 5′) were added, and reactions were incubated for 10 min. Subsequently, 2 µL of 50 mM β-nicotinamide adenine dinucleotide (NAD^+, New England Biolabs) was added, and reactions were allowed to proceed for 1 h at room temperature. Reactions were then split into four aliquots (25 µL each) and supplemented with either 200 µL of Alkaline Lysis Buffer (6 M guanidine-HCl, 50 mM Tris-HCl, pH 8.5) or Acidic Lysis Buffer (6 M guanidine-HCl, 10 mM Tris-HCl, 100 mM sodium phosphate, pH 6.3). For each lysis condition, iodoacetamide (IAA) was either added to a final concentration of 5 mM or omitted. Following lysis and termination of the reactions, samples were split into three aliquots (75 µL each) and subjected to digestion under different conditions: 1 h digestion (“Fast”), 1 h digestion following overnight incubation of the lysed samples (“O/N→Fast”), or overnight digestion (“O/N”). For digestion, alkaline samples were diluted with 150 µL of 50 mM Tris-HCl (pH 8.5), and acidic samples with 150 µL of 100 mM sodium phosphate (pH 6.3), reducing the guanidine-HCl concentration to ~2 M. Both dilution buffers contained Lys-C (333 pg/µL), corresponding to a final Lys-C-to-PARP1 ratio of 1:20 (w/w). Samples were incubated for 30 min at room temperature, followed by further dilution with 75 µL buffer (final guanidine-HCl ~1.5 M) containing sequencing-grade trypsin (666 pg/µL), yielding a trypsin-to-PARP1 ratio of 1:20 (w/w). Digestion proceeded for an additional 30 min before acidification with TFA to 1% (v/v). Acidified samples were purified using C18 StageTips as described above.

MS dataset overview

Dataset 1: Synthetic peptide experiments, related to Figure 1A-D and S1A-B, referred to as “DS1”.
Dataset 2: Benchmarking experiments, related to Figures 2 and 3, referred to as “DS2”.
Dataset 3: Quantitative experiments, related to Figures 4 through 8, referred to as “DS3”.
Dataset 1R: Synthetic peptide experiments (Af1521 incubation), related to Figure 1E and S1C-D, referred to as “DS1R”.
Dataset 2R: Synthetic peptide experiments (Af1521 pulldown), related to Figure 1E and S1E-F, referred to as “DS2R”.
Dataset 3R: Total proteome experiments, related to Figures S5, S6B-D, S7C-D, referred to as “DS3R”.
Dataset 4R: PARP1 in vitro auto-modification experiments, related to Figure S9, referred to as “DS4R”.

ETD-based mass spectrometric analysis

All samples (except total proteome; DS3R) were analyzed using an Orbitrap Fusion™ Lumos™ Tribrid™ mass spectrometer (Thermo), and analyzed on 15-cm long analytical columns with an internal diameter of 75 µm (DS1,2,3) or 50 µm (DS1R,2R,4R), packed in-house using ReproSil-Pur 120 C18-AQ 1.9 µm beads (Dr. Maisch). On-line reversed-phase liquid chromatography to separate peptides was performed using an EASY-nLC™ 1200 system (Thermo) for DS1,2,3, or using a Vanquish™ Neo UHPLC system (Thermo) for DS1R,2R,4R, and the analytical column was heated to 40°C using a column oven (Sonation). For measurement of DS3 samples, n-dodecyl β-D-maltoside (DDM) was added to a final concentration of 0.005%. Peptides were eluted from the column using a gradient of Buffer A (0.1% formic acid) and Buffer B (80% ACN in 0.1% FA). For DS1, the primary gradient ranged from 3% B to 38% B over 18 minutes, followed by a washing block of 7 minutes. For DS1R and DS2R, the primary gradient ranged from 5% B to 28% B over 11 minutes, followed by a washing block of 4 minutes. For DS2 and His10-Af1521 samples from DS3, the primary gradient ranged from 3% B to 24% B over 50 min, followed by a washing block of 30 min, with the times halved for a second acquisition replicate. For GST-Af1521 samples from DS3, the primary gradient ranged from 4% B to 40% B over 35 min, followed by a washing block of 15 min. For DS4R, the primary gradient ranged from 5% B to 40% B over 14 minutes, followed by a washing block of 6 minutes. Electrospray ionization (ESI) was achieved using a Nanospray Flex NG Ion Source (Thermo). Spray voltage was set to 2 kV, capillary temperature to 275°C, and RF level to 40%. Full scans were performed at a resolution of 120,000, with a scan range of 300 to 1,300 m/z (DS1,2,1R,2R,4R) or 350 to 1,250 (DS3), a maximum injection time of 50 ms (DS1,2,3) or 246 ms (DS1R,2R,4R), and an automatic gain control (AGC) target of 600,000 (DS1,2,1R,2R,4R) or 1,000,000 (DS3) charges. Precursors were isolated from the entire full scan range (DS1,1R,2R,4R) or a range of 325 to 1,275 (DS2) or 400 to 1,200 m/z (DS3). Isolation was performed at a width of 1.3 m/z, an AGC target of 200,000 charges, and precursor fragmentation was accomplished using electron transfer disassociation with supplemental higher-collisional disassociation (EThcD) at 20 NCE, using calibrated charge-dependent ETD parameters[78]. Precursors with charge state 2-6 (DS1,1R,2R), 3-5 (DS2,3), or 2-5 (DS4R) were isolated for MS/MS analysis, and for DS2 and DS3 prioritized from charge 3 (highest) to charge 5 (lowest), and for DS4R charge 3-5 were given (equal) top priority, followed by charge 2. Selected precursors were excluded from repeated sequencing by setting a dynamic exclusion of 0.6 s per minute (i.e. 1%) of total gradient time. MS/MS spectra were measured in the Orbitrap at a scan resolution of 60,000, and at various levels of sensitivity. For DS1,2,3, by using TopN and maximum MS2 injection time combinations of: Top5 with 120 ms, Top4 with 180 ms, Top3 with 250 ms, and Top2 with 500 ms. For DS1R,2R,4R, by setting a constant cycle time of 0.8 s (DS1R,2R) or 1.0 s (DS4R) with a maximum MS2 injection time of 250 ms.

Total proteome mass spectrometric analysis

Approximately 1 µg of peptide was analyzed per injection. All total proteome samples (DS3R) were analyzed on a Vanquish™ Neo UHPLC system (Thermo) coupled to an Orbitrap™ Astral™ mass spectrometer (Thermo). Samples were analyzed on 15-cm long analytical columns, with an internal diameter of 50 µm, and packed in-house using ReproSil-Pur 120 C18-AQ 1.9 µm beads (Dr. Maisch). The analytical column was heated to 40 °C, and elution of peptides from the column was achieved by application of gradients with stationary phase Buffer A (0.1% FA) and increasing amounts of mobile phase Buffer B (80% ACN in 0.1% FA). The primary analytical gradient ranged from 10 %B to 38 %B over 22.5 min, followed by a further increase to 48 %B over 2.5 min to elute any remaining peptides, and by a washing block of 3.75 min. Ionization was achieved using a NanoSpray Flex NG ion source (Thermo), with spray voltage set at 2 kV, ion transfer tube temperature to 275 °C, and RF lens to 50%. All full precursor (MS1) scans were acquired using the Orbitrap™ mass analyzer, while all tandem fragment (DIA) scans were acquired in parallel using the Astral™ mass analyzer. Full scan range was set to 300-1,000 m/z, MS1 resolution to 240,000, MS1 AGC target to “500” (5,000,000 charges), and MS1 maximum injection time to 30 ms. Precursors were analyzed in data-independent acquisition (DIA) mode, with isolation window width set to 4 m/z, maximum isolation time set to 5 ms, and DIA AGC target set to “200” (20,000 charges). Precursor mass range for DIA was set to 300-1000 m/z (175 windows) for the first technical replicate, and 302-998 m/z (174 windows) for the second technical replicate. Fragmentation was achieved using higher-energy collision disassociation (HCD) with normalized collision energy of 25, and fragment scan range was set to 150-1,500 m/z. Full scans were performed between each full set of DIA scans, resulting in a cycle time of ~0.9 s.

Synthetic peptide mass spectrometry data analysis

For DS1, 1R, and 2R, analysis of the mass spectrometry raw data was performed using Skyline software[79], version 23.1.0.268. To this end, Skyline was provided with monoisotopic peptide information corresponding to each of the eight peptides, obtained via a pre-search of representative data files using MaxQuant software[80,81], version 1.5.3.30. C-terminal amidation was set as a fixed peptide modification. ADP-ribosylation was set as a variable modification, as well as tryptophan oxidation to kynurenin, as we observed this to be highly prevalent. Thus, Skyline was set up to identify and extract intensity profiles for the following 16 peptide sequences directly from the data.

GWTARKSAEAGTAGK[−1], GW[+4]TARKSAEAGTAGK[−1], GWTAR[+541.1]KSAEAGTAGK[−1], GW[+4]TAR[+541.1]KSAEAGTAGK[−1], GWTARKSAAAGTAGK[−1],

GW[+4]TARKSAAAGTAGK[−1], GWTARKS[+541.1]AAAGTAGK[−1], GW[+4]TARKS[+541.1]AAAGTAGK[−1], GWTARKAAEAGTAGK[−1], GW[+4]TARKAAEAGTAGK[−1], GWTARKAAE[+541.1]AGTAGK[−1], GW[+4]TARKAAE[+541.1]AGTAGK[−1], GWTARKAADAGTAGK[−1], GW[+4]TARKAADAGTAGK[−1], GWTARKAAD[+541.1]AGTAGK[−1], and GW[+4]TARKAAD[+541.1]AGTAGK[−1].

Extracted peptide intensities were normalized to total ion current, and variants of tryptophan oxidation were summed. To calculate the fraction of ADP-ribosylated peptide for each amino acid linkage, the intensity of their respective modified peptide was divided by the summed intensity of both unmodified and modified peptides.

ADP-ribosylome mass spectrometry data analysis

For DS2, DS3, and DS4R, analysis of the mass spectrometry raw data was performed using MaxQuant software[80,81], version 1.5.3.30. MaxQuant default settings were used, with exceptions outlined below. Three separate computational searches were performed, one for each separate MS dataset (DS2,3,4R). For generation of the theoretical spectral library for DS2,3, a HUMAN.fasta database (103,811 entries) was downloaded from UniProt on the 29th of April, 2023. For DS3, the sequence for the Af1521 macrodomain was also included in the search. For DS4R, the PARP1 and PARP1-E988K sequences were used. N-terminal acetylation, methionine oxidation, cysteine carbamidomethylation, and ADP-ribosylation on all amino acid residues known to potentially be modified (C, D, E, H, K, R, S, T, and Y), were included as variable modifications. For the first search, which is only used for mass recalibration, no variable modifications were used. Up to 8 missed cleavages were allowed, a maximum allowance of 3 variable modifications per peptide was used, and maximum peptide mass was set to 6,000 Da. Second peptide search was enabled for DS2 only. For DS2,3, matching between runs (MBR) was enabled with an alignment time window of 20 min, and a match time window of 60 s. Matching was only allowed between same-condition replicates. MBR was not enabled for DS4R. First and main search precursor mass tolerances of 10 and 4.5 ppm were used, respectively. For fragment ion masses, a tolerance of 20 ppm was used. Modified peptides were filtered to have an Andromeda score of >40 (default), and a delta score of >20. A site decoy fraction of 2% was applied. Data was automatically filtered by posterior error probability to achieve a false discovery rate of <1% (default), at the peptide-spectrum match and the protein assignment levels.

Non-specific data search

For DS2, a non-specific data search was performed wherein ADPr is allowed to reside on any of the 20 naturally occurring amino acids, for purposes of validating amino acid specificity and localization potential within the MS data. MaxQuant was used essentially as described above, with the following changes in settings. Maximum missed cleavages were reduced to 4. Only ADP-ribosylation on all 20 amino acids was set as a variable modification, with a maximum of one variable modification per peptide. Maximum peptide mass was restricted to 2,500 Da. Second peptide search was disabled. The “evidence.txt” output file from MaxQuant was used to extract raw localization probabilities.

Data filtering

Beyond automatic filtering and FDR control as applied by MaxQuant, the data were manually stringently filtered in order to ensure proper identification and localization of ADP-ribose. PSMs modified by more than one ADP-ribose were omitted. PSMs corresponding to unique peptides were used for ADP-ribosylation site assignment if localization probability was >0.75. Erroneous MaxQuant intensity assignments were manually corrected in the sites table, and based on localized PSMs only. For ADP-ribosylation target proteins, a list was generated solely based on ADP-ribosylation sites, with multiple sites within the same protein summed up for quantification purposes.

Comparison to other ADPr MS studies

In order to align ADPr target proteins, a scaffold was created based on all unique protein-coding genes as downloaded from UniProt on the 29th of April, 2023. ADPr target proteins identified in this study were aligned to the scaffold, along with ADPr target proteins identified in four other ADPr proteomics studies[7,18,36,37]. Alignment was primarily performed using Uniprot identifier, and otherwise protein-coding gene. For comparison of ADPr sites, a scaffold was generated from all 51 amino acid sequence windows derived from this study, as well as from 51 amino acid sequence windows generated from sites identified in four other ADPr proteomics studies[7,18,36,37]. For the three older studies, since the reported site information did not align with the current version of UniProt, the reported sequence information was re-aligned to the up-to-date UniProt human FASTA file prior to extraction of 51 amino acid sequence windows. Any duplicate 51 amino acid sequences were excluded, and afterwards all studies were individually mapped to the scaffold.

Total proteome mass spectrometry data analysis

For total proteome samples (DS3R), analysis of the mass spectrometry raw data was performed using DIA-NN[82], v1.9.2. For library-free search, the human FASTA database (105,529 entries) was

downloaded from UniProt on the 13th of November, 2024, and DIA-NN was used to generate a spectral library in silico. To this end, settings used were Trypsin/P digestion (default), 2 missed cleavages, peptide length between 6 and 60, precursor charge state between 2 and 4, precursor m/z range from 300 to 1,000 m/z, and fragment ion m/z range from 100 to 1,500 m/z. RAW files were first converted to DIA format, after which they were searched with DIA-NN using the spectral library described above, with default settings. “MBR” was enabled, which generates a new spectral library based on a first search, which is then used to re-analyze the data. Global false discovery rate control was set to 1% (default). The “--matrix-spec-q” command was provided, to enforce a 1% FDR control at the run-specific level (in addition to the global FDR control). For further processing, the “report.gg_matrix.tsv” file was used, which collapses identifications into gene groups (i.e. protein-coding genes). Two technical replicates were analyzed per sample, and their intensity values were summed.

Quantification and statistical analysis

Details regarding the statistical analysis can be found in the respective figure legends. All quantitative experiments were performed using at least four replicates to ensure sufficient statistical power. Statistical handling of the data was primarily performed using the freely available Perseus software[83], version 1.5.5.3, and includes term enrichment analysis through FDR-controlled Fisher Exact testing, scatter plot analysis and linear regression, data normalization, imputation, volcano plot analysis (using permutation-based FDR control and an s0 value of 0.5), hierarchical clustering, and principle component analysis. ADPr site intensity values were primarily derived through MS/MS intensity values as reported by MaxQuant, derived from “evidence.txt”, with only localized (>0.75) values considered for quantification. Matching between runs (MBR) intensity values were considered based on matching between same-condition replicates, i.e. matching of MS1-based evidence across different experimental condition was disallowed. ADPr site intensity values were median-normalized across all same-condition replicates, and ADPr sites were only considered quantifiable if detectable in n=4/4 in at least one experiment condition. Following this, any missing values were imputed using random values sampled from below the overall experimental detection limit (down shift 1.8, width 0.3). Visualization of the Af1521 structure was performed using ChimeraX[84], version 1.9. Venn diagram overlaps were performed using Venny 2.1 (https://bioinfogp.cnb.csic.es/tools/venny/), and scaled Venn diagrams were rendered using eulerAPE 3.0 (https://www.eulerdiagrams.com/eulerAPE/v2/). UpSet plots were generated using ChiPlot (https://www.chiplot.online/upset_plot.html). Boxplots were drawn using BoxPlotR (http://shiny.chemgrid.org/boxplotr/). Protter visualization was generated using Protter[85], version 1.0. Interconnected protein networks were acquired using the STRING database[86], version 12.0,

and the layout was designed using Cytoscape[87], version 3.10.3. Plotting of graphs was done using either Perseus, GraphPad Prism version 11, or Microsoft Excel (Office Professional Plus 2016). All art was drawn and all graphs were polished using Adobe Illustrator CS6.

DATA AVAILABILITY

The mass spectrometry proteomics data generated in this study have been deposited in the ProteomeXchange Consortium via the PRIDE[88] partner repository, with the dataset identifiers PXD070310 (datasets 1, 2, and 3) and PXD075810 (datasets 1R, 2R, 3R, and 4R).

PXD070310 [http://proteomecentral.proteomexchange.org/cgi/GetDataset?ID=PXD070310]
PXD075810 [http://proteomecentral.proteomexchange.org/cgi/GetDataset?ID=PXD075810]

The following PDB structures are referred to:
2BFQ [https://doi.org/10.2210/pdb2BFQ/pdb]
1UBQ [https://doi.org/10.2210/pdb1UBQ/pdb]

Representative annotated MS/MS spectra are provided as Supplementary Data 9. All other data generated in this study are provided in the Supplementary Data files. Source data are provided with this paper.

REFERENCES

1. Luscher B, Butepage M, Eckei L, Krieg S, Verheugd P, Shilton BH. ADP-Ribosylation, a Multifaceted Posttranslational Modification Involved in the Control of Cell Physiology in Health and Disease. *Chem Rev* **118**, 1092-1136 (2018).

2. Suskiewicz MJ, Prokhorova E, Rack JGM, Ahel I. ADP-ribosylation from molecular mechanisms to therapeutic implications. *Cell* **186**, 4475-4495 (2023).

3. Luscher B*, et al.* ADP-ribosyltransferases, an update on function and nomenclature. *FEBS J* **289**, 7399-7410 (2022).

4. Chambon P, Weill JD, Mandel P. Nicotinamide mononucleotide activation of new DNA-dependent polyadenylic acid synthesizing nuclear enzyme. *Biochem Biophys Res Commun* **11**, 39-43 (1963).

5. Olsen JV, Mann M. Status of large-scale analysis of post-translational modifications by mass spectrometry. *Mol Cell Proteomics* **12**, 3444-3452 (2013).

6. Larsen SC, Hendriks IA, Lyon D, Jensen LJ, Nielsen ML. Systems-wide Analysis of Serine ADP-Ribosylation Reveals Widespread Occurrence and Site-Specific Overlap with Phosphorylation. *Cell Rep* **24**, 2493-2505 e2494 (2018).

7. Zhang Y, Wang J, Ding M, Yu Y. Site-specific characterization of the Asp- and Glu-ADP-ribosylated proteome. *Nat Methods* **10**, 981-984 (2013).

8. Daniels CM, Ong SE, Leung AK. Phosphoproteomic approach to characterize protein mono- and poly(ADP-ribosyl)ation sites from cells. *J Proteome Res* **13**, 3510-3522 (2014).

9. Martello R*, et al.* Proteome-wide identification of the endogenous ADP-ribosylome of mammalian cells and tissue. *Nat Commun* **7**, 12917 (2016).

10. Bilan V, Leutert M, Nanni P, Panse C, Hottiger MO. Combining Higher-Energy Collision Dissociation and Electron-Transfer/Higher-Energy Collision Dissociation Fragmentation in a Product-Dependent Manner Confidently Assigns Proteomewide ADP-Ribose Acceptor Sites. *Anal Chem* **89**, 1523-1530 (2017).

11. Gagné JP*, et al.* Quantitative site-specific ADP-ribosylation profiling of DNA-dependent PARPs. *DNA Repair (Amst)* **30**, 68-79 (2015).

12. Hendriks IA, Larsen SC, Nielsen ML. An Advanced Strategy for Comprehensive Profiling of ADP-ribosylation Sites Using Mass Spectrometry-based Proteomics. *Mol Cell Proteomics* **18**, 1010-1026 (2019).

13. Bonfiglio JJ*, et al.* Serine ADP-Ribosylation Depends on HPF1. *Mol Cell* **65**, 932-940 (2017).

14. Fontana P, Bonfiglio JJ, Palazzo L, Bartlett E, Matic I, Ahel I. Serine ADP-ribosylation reversal by the hydrolase ARH3. *Elife* **6**, (2017).

15. Palazzo L, Leidecker O, Prokhorova E, Dauben H, Matic I, Ahel I. Serine is the major residue for ADP-ribosylation upon DNA damage. *Elife* **7**, (2018).

16. Suskiewicz MJ*, et al.* HPF1 completes the PARP active site for DNA damage-induced ADP-ribosylation. *Nature* **579**, 598-602 (2020).

17. Tashiro K*, et al.* Chemoenzymatic and Synthetic Approaches To Investigate Aspartate- and Glutamate-ADP-Ribosylation. *J Am Chem Soc* **145**, 14000-14009 (2023).

18. Longarini EJ, Matic I. Preserving ester-linked modifications reveals glutamate and aspartate mono-ADP-ribosylation by PARP1 and its reversal by PARG. *Nat Commun* **15**, 4239 (2024).

19. Javed Z*, et al.* Using TLC-MALDI-TOF to Interrogate In Vitro Peptidyl Proximal Preferences of PARP14 and Glycohydrolase Specificity. *Molecules* **28**, (2023).

20. Buch-Larsen SC*, et al.* Mapping Physiological ADP-Ribosylation Using Activated Ion Electron Transfer Dissociation. *Cell Rep* **32**, 108176 (2020).

21. Rosenthal F*, et al.* Macrodomain-containing proteins are new mono-ADP-ribosylhydrolases. *Nat Struct Mol Biol* **20**, 502-507 (2013).

22. Jankevicius G*, et al.* A family of macrodomain proteins reverses cellular mono-ADP-ribosylation. *Nat Struct Mol Biol* **20**, 508-514 (2013).

23. Nowak K*, et al.* Engineering Af1521 improves ADP-ribose binding and identification of ADP-ribosylated proteins. *Nat Commun* **11**, 5199 (2020).

24. Garcia-Saura AG, Herzog LK, Dantuma NP, Schuler H. MacroGreen, a simple tool for detection of ADP-ribosylated proteins. *Commun Biol* **4**, 919 (2021).

25. Ribeiro VC, Russo LC, Hoch NC. PARP14 is regulated by the PARP9/DTX3L complex and promotes interferon gamma-induced ADP-ribosylation. *EMBO J* **43**, 2908-2928 (2024).

26. Kar P*, et al.* PARP14 and PARP9/DTX3L regulate interferon-induced ADP-ribosylation. *EMBO J* **43**, 2929-2953 (2024).

27. Leidecker O*, et al.* Serine is a new target residue for endogenous ADP-ribosylation on histones. *Nat Chem Biol* **12**, 998-1000 (2016).

28. Liu Q, Florea BI, Filippov DV. ADP-Ribosylation Goes Normal: Serine as the Major Site of the Modification. *Cell Chem Biol* **24**, 431-432 (2017).

29. Langelier MF, Billur R, Sverzhinsky A, Black BE, Pascal JM. HPF1 dynamically controls the PARP1/2 balance between initiating and elongating ADP-ribose modifications. *Nat Commun* **12**, 6675 (2021).

30. Rudolph J, Roberts G, Muthurajan UM, Luger K. HPF1 and nucleosomes mediate a dramatic switch in activity of PARP1 from polymerase to hydrolase. *Elife* **10**, (2021).

31. Hendriks IA*, et al.* The regulatory landscape of the human HPF1- and ARH3-dependent ADP-ribosylome. *Nat Commun* **12**, 5893 (2021).

32. Glowacki G*, et al.* The family of toxin-related ecto-ADP-ribosyltransferases in humans and the mouse. *Protein Sci* **11**, 1657-1670 (2002).

33. Gibbs-Seymour I, Fontana P, Rack JGM, Ahel I. HPF1/C4orf27 Is a PARP-1-Interacting Protein that Regulates PARP-1 ADP-Ribosylation Activity. *Mol Cell* **62**, 432-442 (2016).

34. Garcia-Saura AG, Schuler H. PARP10 Multi-Site Auto- and Histone MARylation Visualized by Acid-Urea Gel Electrophoresis. *Cells* **10**, (2021).

35. Kaufmann M, Feijs KL, Luscher B. Function and regulation of the mono-ADP-ribosyltransferase ARTD10. *Curr Top Microbiol Immunol* **384**, 167-188 (2015).

36. Gibson BA*, et al.* Chemical genetic discovery of PARP targets reveals a role for PARP-1 in transcription elongation. *Science* **353**, 45-50 (2016).

37. Zhen Y, Zhang Y, Yu Y. A Cell-Line-Specific Atlas of PARP-Mediated Protein Asp/Glu-ADP-Ribosylation in Breast Cancer. *Cell Rep* **21**, 2326-2337 (2017).

38. Dukic N*, et al.* PARP14 is a PARP with both ADP-ribosyl transferase and hydrolase activities. *Sci Adv* **9**, eadi2687 (2023).

39. Verheugd P*, et al.* Regulation of NF-kappaB signalling by the mono-ADP-ribosyltransferase ARTD10. *Nat Commun* **4**, 1683 (2013).

40. Zhu K*, et al.* DELTEX E3 ligases ubiquitylate ADP-ribosyl modification on protein substrates. *Sci Adv* **8**, eadd4253 (2022).

41. Bejan DS, Lacoursiere RE, Pruneda JN, Cohen MS. Ubiquitin is directly linked via an ester to protein-conjugated mono-ADP-ribose. *EMBO J* **44**, 2211-2231 (2025).

42. Kolvenbach A, Palumbieri MD, Colby T, Nadarajan D, Bode R, Matic I. Serine ADPr on histones and PARP1 is a cellular target of ester-linked ubiquitylation. *Nat Chem Biol*, (2025).

43. Chatrin C, Zhu K, Ahel I. The rise of ADP-ribose-ubiquitin. *Nat Struct Mol Biol* **32**, 1582-1585 (2025).

44. Tang L, Liu X, Wang C, Shu C. USP18 promotes innate immune responses and apoptosis in influenza A virus-infected A549 cells via cGAS-STING pathway. *Virology* **585**, 240-247 (2023).

45. Wang Y*, et al.* Positive Feedback Loop of Long Noncoding RNA OASL-IT1 and Innate Immune Response Restricts the Replication of Zika Virus in Epithelial A549 Cells. *J Innate Immun* **13**, 179-193 (2021).

46. Dias AA*, et al.* TLR-9 Plays a Role in Mycobacterium leprae-Induced Innate Immune Activation of A549 Alveolar Epithelial Cells. *Front Immunol* **12**, 657449 (2021).

47. Szklarczyk D*, et al.* The STRING database in 2023: protein-protein association networks and functional enrichment analyses for any sequenced genome of interest. *Nucleic Acids Res* **51**, D638-D646 (2023).

48. Luscher B, Verheirstraeten M, Krieg S, Korn P. Intracellular mono-ADP-ribosyltransferases at the host-virus interphase. *Cell Mol Life Sci* **79**, 288 (2022).

49. Malgras M, Garcia M, Jousselin C, Bodet C, Leveque N. The Antiviral Activities of Poly-ADP-Ribose Polymerases. *Viruses* **13**, (2021).

50. Liu Q, Peng S, Wei J, Xie Z. The Function of TRIM25 in Antiviral Defense and Viral Immune Evasion. *Viruses* **17**, (2025).

51. Buch-Larsen SC, Rebak A, Hendriks IA, Nielsen ML. Temporal and Site-Specific ADP-Ribosylation Dynamics upon Different Genotoxic Stresses. *Cells* **10**, (2021).

52. Leung AK. SERious Surprises for ADP-Ribosylation Specificity: HPF1 Switches PARP1 Specificity to Ser Residues. *Mol Cell* **65**, 777-778 (2017).

53. Jungmichel S, Rosenthal F, Altmeyer M, Lukas J, Hottiger MO, Nielsen ML. Proteome-wide identification of poly(ADP-Ribosyl)ation targets in different genotoxic stress responses. *Mol Cell* **52**, 272-285 (2013).

54. Voorneveld J*, et al.* Arginine ADP-Ribosylation: Chemical Synthesis of Post-Translationally Modified Ubiquitin Proteins. *J Am Chem Soc* **144**, 20582-20589 (2022).

55. Moss J, Yost DA, Stanley SJ. Amino acid-specific ADP-ribosylation. *J Biol Chem* **258**, 6466-6470 (1983).

56. Hsia JA, Tsai SC, Adamik R, Yost DA, Hewlett EL, Moss J. Amino acid-specific ADP-ribosylation. Sensitivity to hydroxylamine of [cysteine(ADP-ribose)]protein and [arginine(ADP-ribose)]protein linkages. *J Biol Chem* **260**, 16187-16191 (1985).

57. McDonald LJ, Moss J. Enzymatic and nonenzymatic ADP-ribosylation of cysteine. *Mol Cell Biochem* **138**, 221-226 (1994).

58. Perrard J, Smith S. Multiple E3 ligases control tankyrase stability and function. *Nat Commun* **14**, 7208 (2023).

59. Rodriguez KM*, et al.* Chemical genetics and proteome-wide site mapping reveal cysteine MARylation by PARP-7 on immune-relevant protein targets. *Elife* **10**, (2021).

60. Groslambert J, Schutzenhofer K, Palazzo L, Ahel I. PARPs and ADP-ribosyl hydrolases in cancer therapy: From drug targets to biomarkers. *DNA Repair (Amst)* **152**, 103863 (2025).

61. O'Sullivan J*, et al.* Emerging roles of eraser enzymes in the dynamic control of protein ADP-ribosylation. *Nat Commun* **10**, 1182 (2019).

62. Agrata R, Komander D. Ubiquitin-A structural perspective. *Mol Cell* **85**, 323-346 (2025).

63. Dikic I, Schulman BA. An expanded lexicon for the ubiquitin code. *Nat Rev Mol Cell Biol* **24**, 273-287 (2023).

64. Kleine H*, et al.* Dynamic subcellular localization of the mono-ADP-ribosyltransferase ARTD10 and interaction with the ubiquitin receptor p62. *Cell Commun Signal* **10**, 28 (2012).

65. Yang CS*, et al.* Ubiquitin Modification by the E3 Ligase/ADP-Ribosyltransferase Dtx3L/Parp9. *Mol Cell* **66**, 503-516 e505 (2017).

66. Zhu K, Chatrin C, Smith R, Ahel D, Ahel I. Interplay between ubiquitination and ADP-ribosylation and the case of dual modification ADPr-Ub. *Essays Biochem*, (2025).

67. Zhu K*, et al.* DELTEX E3 ligases ubiquitylate ADP-ribosyl modification on nucleic acids. *Nucleic Acids Res* **52**, 801-815 (2024).

68. Kloet MS*, et al.* Identification of RNF114 as ADPr-Ub reader through non-hydrolysable ubiquitinated ADP-ribose. *Nat Commun* **16**, 6319 (2025).

69. Lacoursiere RE*, et al.* A family of E3 ligases extend K11 polyubiquitin on sites of MARUbylation. *bioRxiv*, (2025).

70. Daniels CM*, et al.* Dynamic ADP-Ribosylome, Phosphoproteome, and Interactome in LPS-Activated Macrophages. *J Proteome Res* **19**, 3716-3731 (2020).

71. Thirunavukkarasu S*, et al.* Poly(ADP-ribose) polymerase 9 mediates early protection against Mycobacterium tuberculosis infection by regulating type I IFN production. *J Clin Invest* **133**, (2023).

72. Parthasarathy S*, et al.* PARP14 is an interferon-induced host factor that promotes IFN production and affects the replication of multiple viruses. *mBio* **16**, e0229925 (2025).

73. Zhang Z*, et al.* Global remodeling of ADP-ribosylation by PARP1 suppresses influenza A virus infection. *Nat Commun* **16**, 11176 (2025).

74. Megger DA, Philipp J, Le-Trilling VTK, Sitek B, Trilling M. Deciphering of the Human Interferon-Regulated Proteome by Mass Spectrometry-Based Quantitative Analysis Reveals Extent and Dynamics of Protein Induction and Repression. *Front Immunol* **8**, 1139 (2017).

75. Raja R*, et al.* Interferon-induced PARP14-mediated ADP-ribosylation in p62 bodies requires the ubiquitin-proteasome system. *EMBO J*, (2025).

76. Herzog N*, et al.* Caspase-dependent cleavage of the mono-ADP-ribosyltransferase ARTD10 interferes with its pro-apoptotic function. *FEBS J* **280**, 1330-1343 (2013).

77. Tashiro K, Mohapatra J, Brautigam CA, Liszczak G. A Protein Semisynthesis-Based Strategy to Investigate the Functional Impact of Linker Histone Serine ADP-Ribosylation. *ACS Chem Biol* **17**, 810-815 (2022).

78. Rose CM*, et al.* A calibration routine for efficient ETD in large-scale proteomics. *J Am Soc Mass Spectrom* **26**, 1848-1857 (2015).

79. Pino LK, Searle BC, Bollinger JG, Nunn B, MacLean B, MacCoss MJ. The Skyline ecosystem: Informatics for quantitative mass spectrometry proteomics. *Mass Spectrom Rev* **39**, 229-244 (2020).

80. Cox J, Neuhauser N, Michalski A, Scheltema RA, Olsen JV, Mann M. Andromeda: a peptide search engine integrated into the MaxQuant environment. *J Proteome Res* **10**, 1794-1805 (2011).

81. Cox J, Mann M. MaxQuant enables high peptide identification rates, individualized p.p.b.-range mass accuracies and proteome-wide protein quantification. *Nat Biotechnol* **26**, 1367-1372 (2008).

82. Demichev V, Messner CB, Vernardis SI, Lilley KS, Ralser M. DIA-NN: neural networks and interference correction enable deep proteome coverage in high throughput. *Nat Methods* **17**, 41-44 (2020).

83. Tyanova S*, et al.* The Perseus computational platform for comprehensive analysis of (prote)omics data. *Nat Methods* **13**, 731-740 (2016).

84. Meng EC*, et al.* UCSF ChimeraX: Tools for structure building and analysis. *Protein Sci* **32**, e4792 (2023).

85. Omasits U, Ahrens CH, Muller S, Wollscheid B. Protter: interactive protein feature visualization and integration with experimental proteomic data. *Bioinformatics* **30**, 884-886 (2014).

86. Szklarczyk D*, et al.* STRING v11: protein-protein association networks with increased coverage, supporting functional discovery in genome-wide experimental datasets. *Nucleic Acids Res* **47**, D607-D613 (2019).

87. Shannon P*, et al.* Cytoscape: a software environment for integrated models of biomolecular interaction networks. *Genome Res* **13**, 2498-2504 (2003).

88. Perez-Riverol Y*, et al.* The PRIDE database and related tools and resources in 2019: improving support for quantification data. *Nucleic Acids Res* **47**, D442-D450 (2019).

89. Bekker-Jensen DB*, et al.* An Optimized Shotgun Strategy for the Rapid Generation of Comprehensive Human Proteomes. *Cell Syst* **4**, 587-599 (2017).

ACKNOWLEDGEMENTS

We would like to thank members of the NNF-CPR Mass Spectrometry Platform for instrument support and technical assistance, and the lab of Michael O. Hottiger (University of Zurich) for the expression and purification of recombinant human PARG.

FUNDING

The work carried out in this study was in part supported by the Novo Nordisk Foundation Center for Protein Research, the Novo Nordisk Foundation (grant agreement numbers NNF14CC0001, NNF13OC0006477, and NNF24SA0098829), Danish Council of Independent Research (grant agreement numbers 8020-00220B and 0135-00096B), The Danish Cancer Society (grant agreement R146-A9159-16-S2), a center-of-excellence grant from the Danish National Research Foundation to Copenhagen Center for Glycocalyx Research (DNRF196), the Wellcome Trust (223107 and 302632), the Biotechnology and Biological Sciences Research Council (BB/R007195/1 and BB/W016613/1), and Cancer Research UK (C35050/A22284).

AUTHOR CONTRIBUTIONS

S.C.B-L., I.A.H, I.A, and M.L.N. conceived the project. K.T. and G.L. prepared synthetic ADPr peptides. S.C.B-L. and I.A.H. prepared all samples, measured all samples on the mass spectrometer (MS), processed all MS raw data, and performed MS data analysis. J.D.E. assisted with MS data analysis. S.C.B-L. and I.A.H. prepared all figures and wrote the first draft of the manuscript. B.L. supplied PARP10-inducible cells and provided consult. S.Y.V., J.V.O., and M.L.N. provided mass spectrometer infrastructure. S.C.B-L., I.A.H., and I.A. finalized the manuscript with input from all authors.

COMPETING INTERESTS

The authors declare no conflict of interest.

FIGURE LEGENDS

Figure 1. MS-based evaluation of stability of ADPr linked to Asp, Glu, Arg, and Ser residues. (A) Summary of the strategy employed. Synthetic peptides bearing specific APDr linkages were incubated in a variety of ways, prior to analysis using ETD-based mass spectrometry. Sample tube art adapted from Servier Medical Art (https://smart.servier.com), licensed under CC BY 4.0 (https://creativecommons.org/licenses/by/4.0/). (B) Relative stability of ADPr linkages over time at 7 °C, normalized to timepoint 0. Median values are indicated, *n*=7 technical replicates. (C) Relative ADPr stability across different pH values across common MS buffers at room temperature, prior to

vacuum drying and analysis, *n*=4 technical replicates. (D) Relative ADPr stability at different pH, temperature, and in the absence of presence of Af1521 macrodomain ("MD"). *n*=4 technical replicates. (E) Relative ADPr stability in the presence of WT and mutant (K35E / Y145R) Af1521, at different pH, temperature, and incubation times. Modified peptide fractions were normalized to the stock control (left-most dataset). *n*=6 technical replicates. (F) As **E**, but with the stability experiment followed up by a series of Af1521-bead washes to mimic pulldown conditions. Data is expressed as the fraction of input modified ADPr peptides recovered following pulldown and elution. *n*=6 technical replicates.

Figure 2. Benchmarking different proteomics workflows for purification of any ADPr linkage type. (A) Experimental design overview. Different cell lines were treated as indicated, prior to lysis and further processing under either predominantly alkaline conditions, or exclusively acidic conditions. Following proteolytic digestion, peptides were treated with PARG or not, and enrichment of ADPr was performed using either wildtype of mutant Af1521 macrodomain. (B) Structure of the Af1521 macrodomain, as reproduced from PDB structure 2BFQ. The location of a bound ADPr moiety, as well as the Lys-35 and Tyr-145 residues that are mutated in the engineered macrodomain[23,24], are indicated. (C) Overview of the cumulative number of ADPr sites identified in the A549 +IFNγ samples, with distribution of amino acid types indicated. (D) As **C**, but for HeLa +H_2O_2 samples. (E) As **C**, but for U2OS ΔHPF1 +H_2O_2 samples.

Figure 3. Distribution of different ADPr linkages across different cell lines and treatments. (A) Total number of ADPr sites identified in the benchmark experiment, for the five most observed linkages. (B) Scaled Venn diagram showing overlap between the different cell types and treatments, for either Ser ADPr sites (top) or Ser ADPr target proteins (bottom). (C) As **B**, but for Asp and Glu ADPr. (D) Term enrichment analysis, where the Gene Ontology subcellular localization was compared for subsets of ADPr target proteins, versus the background total proteome. Positive enrichment ratio indicates a higher-than-expected observation of ADPr target proteins within the category. * p<0.05, *** p<0.0001, determined via two-tailed Fisher Exact testing with Benjamini-Hochberg correction for multiple-hypotheses testing. Faded bars lack statistical significance. Exact p-values, from left to right: $2.2*10^{-7}$, $2.8*10^{-5}$, 1, 1, $1.3*10^{-12}$, 1, 1, $6.0*10^{-6}$, 1, 0.44, $4.6*10^{-96}$, $4.3*10^{-6}$, 0.70, $9.5*10^{-21}$, 0.031, 1, $5.7*10^{-10}$, 1.

Figure 4. Quantitative profiling of labile ADPr sites in the context of cytokine treatment. (A) Overview of the experimental design. Briefly, A549 and HeLa cells were cultured in quadruplicates, and treated as indicated. PARP10 was induced in HeLa cells using 1 µg/mL doxycycline for 24 h.

IFNα treatment; 24 h with 0.684 ng/mL (~180 U/mL), IFNγ treatment; 24 h with 100 ng/mL (~194 U/mL), TNFα treatment; 6 h with 5 ng/mL (~196 U/mL). Lysis and further processing was performed under exclusively acidic conditions, with enrichment using mutant Af1521, to preserve labile ADPr linkages. Analysis was performed using ETD-based mass spectrometry, *n*=4 cell culture replicates. (B) Overview of the total number of ADPr sites and target proteins identified across the quantitative experiment. (C) Number of ADPr sites identified per experimental condition, either directly within each sample (MS/MS), or after matching of MS-based evidence between same-condition replicates (MBR). Error bars represent s.d., *n*=4 cell culture replicates. (D) As **C**, but visualizing total abundance of ADPr site signal. Error bars represent s.d., *n*=4 cell culture replicates. (E) 'Spiderman' plot, visualizing the relative distribution of each residue-specific ADPr to the total ADPr within the experiment, either when considering the number of sites (left plot), or when going by summed abundance (right plot). A549 conditions are visualized at the top, and HeLa conditions at the bottom.

Figure 5. Reproducibility analysis and comparing to previous Glu/Asp ADPr studies. (A) Unsupervised hierarchical clustering analysis, resulting in a heatmap which displays the overall presence or absence of ADPr target proteins as identified across all replicates and conditions. Summed ADPr site abundances were z-score normalized prior to Euclidian clustering. (B) Principle component analysis, visualizing the greatest degrees of variance (component 1 followed by component 2) within the entire dataset. (C) UpSet analysis for ADPr sites (top-right), UpSet analysis for ADPr target proteins (bottom-left), and depth of sequencing analysis (central). The UpSet analyses demonstrate which studies, or combinations of studies, (co-)identified the most ADPr sites or proteins, with the top 25 most occurring combinations visualized. The depth of sequencing is a boxplot visualization of the iBAQ protein expression values, derived from Bekker-Jensen et al.[89], for all ADPr target proteins identified in each study. Thick line; median, dashed line; mean, box limits; 1st and 3rd quartile, whisker limits; 5th and 95th percentile. The number below the boxes denotes the number of ADPr target proteins (i.e. *n*) within the study. Previously published ADPr data were adapted from Zhang et al.[7], Gibson et al.[36], Zhen et al.[37], and Longarini and Matic[18].

Figure 6. PARP10 expression induces ubiquitin ADP-ribosylation and ADPr-ubiquitylation. (A) Volcano plot analysis, visualizing ADPr target protein dynamics between PARP10-induced (right) and control (left). The significance cut-off line is drawn at *q*=0.01. Significance determined via student's two-sided t-testing with permutation-based FDR control, *n*=4 cell culture replicates. (B) As **A**, but for PARP10-induced +IFNα (right) versus PARP10 (left). The significance cut-off line

is drawn at *q*=0.01. Significance determined via student's two-sided t-testing with permutation-based FDR control, *n*=4 cell culture replicates. (C) Overview of the top five most abundantly ADPr proteins in HeLa cells, following PARP10 induction. Number and abundance (in arbitrary units) of Glu/Asp and Ser ADPr, and overall ratio of change in modification, is indicated for each of the proteins. (D) Overview of all ADPr sites detected on ubiquitin, and their abundance (in arbitrary units), in control and PARP10-induced cells. "CT"; carboxyl terminus. (E) Linear visualization of ubiquitin with ADPr sites highlighted. "CT"; carboxyl terminus. (F) Structure of ubiquitin, as reproduced from PDB structure 1UBQ, with the three ADPr sites most prominently induced on PARP10 induction highlighted. (G) Fully annotated MS/MS spectrum, corresponding to a peptide from ubiquitin, modified by ADP-ribosylation on the most C-terminal Glu residue, with that ADPr itself modified by ubiquitin as determined via the di-glycine remnant still residing on the ADPr following trypsin digestion. Pinpoint localization of ADPr-ubiquitylation is highlighted via subtraction of the $z°_4$ and $z°_3$ ions, as well as subtraction of the c_{15} and c_{12} ions (which also includes the asparagine and valine residues), with observed mass differences matching the expected monoisotopic shifts. This essentially demonstrates ubiquitin-ADPr-ubiquitin tethered together, i.e. Ub-ADPr-Ub.

Figure 7. Interferon treatment induces a robust Glu/Asp/Cys ADPr response in A549 cells. (A) Scatter plot analysis, visualizing the ADP-ribosylation ratio of change of target proteins for IFNα (x-axis) and IFNγ (y-axis) treatment of A549 cells, in both cases compared versus untreated cells. Coloring of the proteins and labels indicates statistical significance (*q*<0.01); purple is both, yellow is IFNα, and green is IFNγ. Significance determined via student's two-sided t-testing with permutation-based FDR control, *n*=4 cell culture replicates. (B) Volcano plot analysis, visualizing ADPr sites stratified by amino acid residue, with the cut-off line at *q*=0.01. Significance determined via student's two-sided t-testing with permutation-based FDR control, *n*=4 cell culture replicates. The boxplot visualization below summarizes all data points on the x-axis for each amino acid residue. Thick line; median, plus symbol; mean, box limits; 1st and 3rd quartile, whisker limits; 5th and 95th percentile. (C) STRING network analysis of all ADPr target proteins that were significantly upregulated both in response to IFNα and IFNγ. 96 out of 102 proteins were interconnected at default STRING clustering confidence, the 6 disconnected nodes are not shown. Node coloring represents relative contribution of each ADPr amino acid linkage type to overall protein modification, size corresponds to number of sites, label font type indicates cytoplasmic, vesicle, or other localization, and thick node outline indicates the protein is annotated by Reactome as involved in "Infectious Disease". All annotated terms are significantly enriched within the network, as determined by the STRING database, compared to the total proteome background.

Figure 8. Interferon treatment induces a robust Glu/Asp/Cys ADPr response in A549 cells. (A) Heatmap analysis, displaying how prominently the different PARP family members were detected as ADP-ribosylated across all replicates and conditions. Summed ADPr site abundances were z-scored prior to plotting. (B) Scatter plot analysis, visualizing the ADP-ribosylation ratio of change of ADPr target proteins in response to IFNα treatment in A549 cells (x-axis) and HeLa cells (y-axis), compared versus their respective controls. Coloring of the proteins and labels indicates significance (q<0.01); purple is both, red is A549, and blue is HeLa. Significance determined via student's two-sided t-testing with permutation-based FDR control, n=4 cell culture replicates. (C) STRING network analysis of all 15 ADPr target proteins that were significantly upregulated in response to IFNα, both in A549 and HeLa cells. Coloring represents how highly ADPr is induced upon IFNα treatment, with inner node color for A549 and outer node color for HeLa. Size of the nodes scales to the number of ADPr sites per protein. (D) Linear visualization of the PARP proteins from **B** and **C**. Drawings are scaled to the length of the proteins, with known domains indicated. All mapped ADPr sites are marked, stratified by detection in A549 or HeLa. Small stars indicate 5-25% of total protein ADPr detected on the residue, whereas large stars indicate >25% of protein ADPr on the residue.

Editor's Summary

Labile ADP-ribosylation has remained challenging to study. Here, the authors develop a mass spectrometry workflow that enables mapping of these modifications and reveals roles in immune and antiviral signaling.

Peer Review Information: *Nature Communications* thanks the anonymous reviewer(s) for their contribution to the peer review of this work. A peer review file is available.

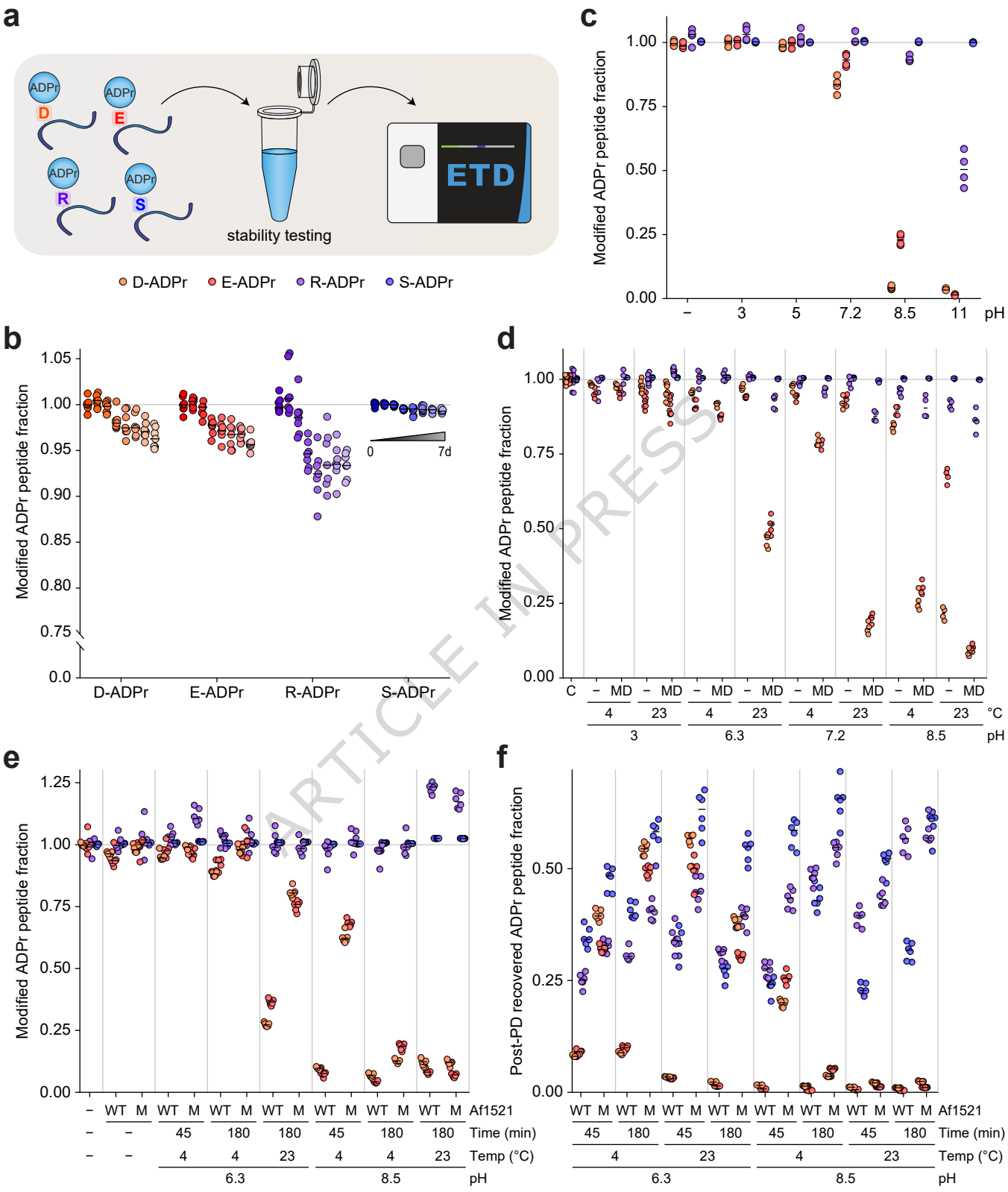

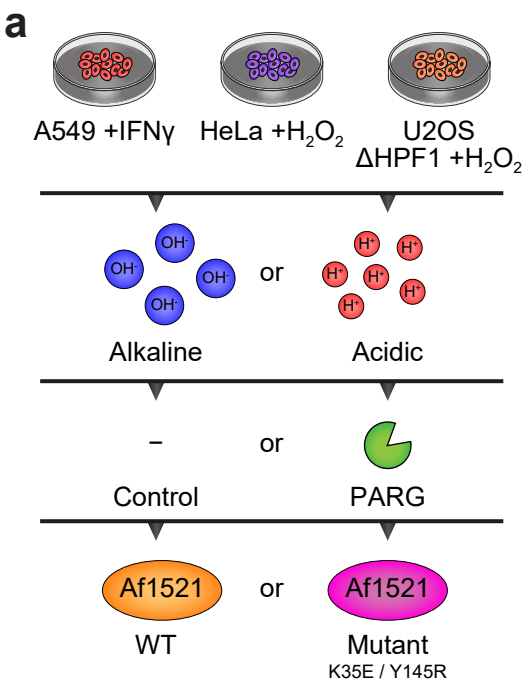

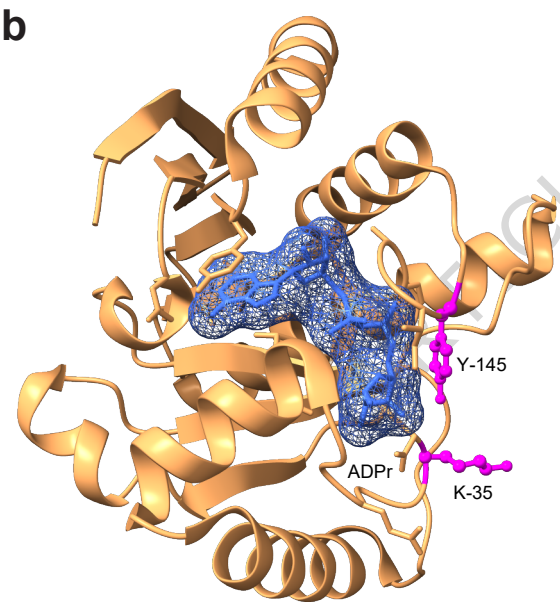

Af1521 (PDB: 2BFQ)

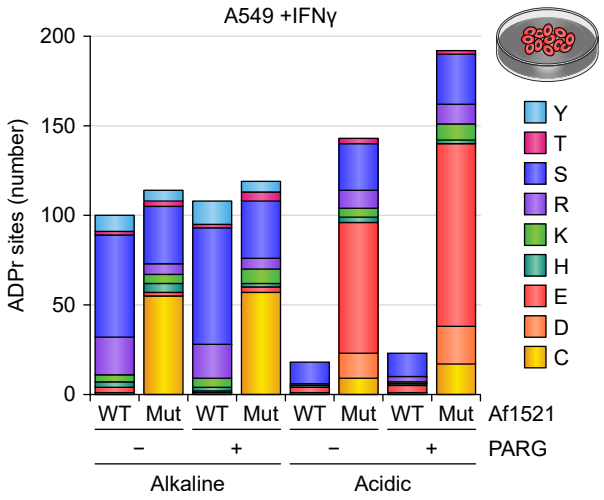

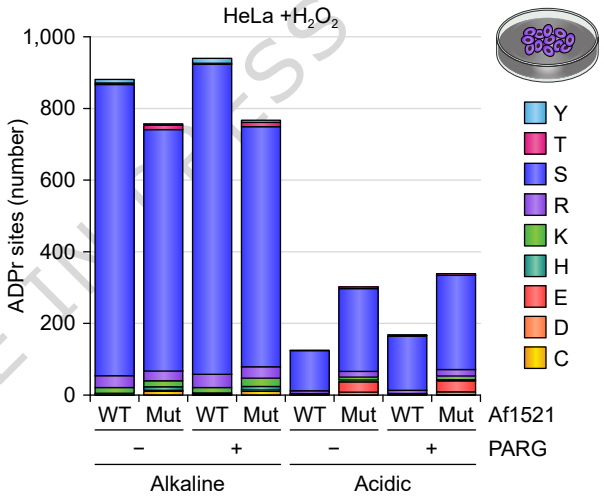

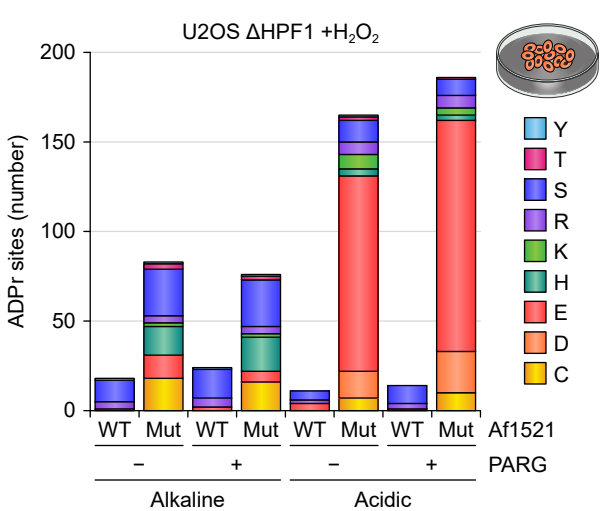

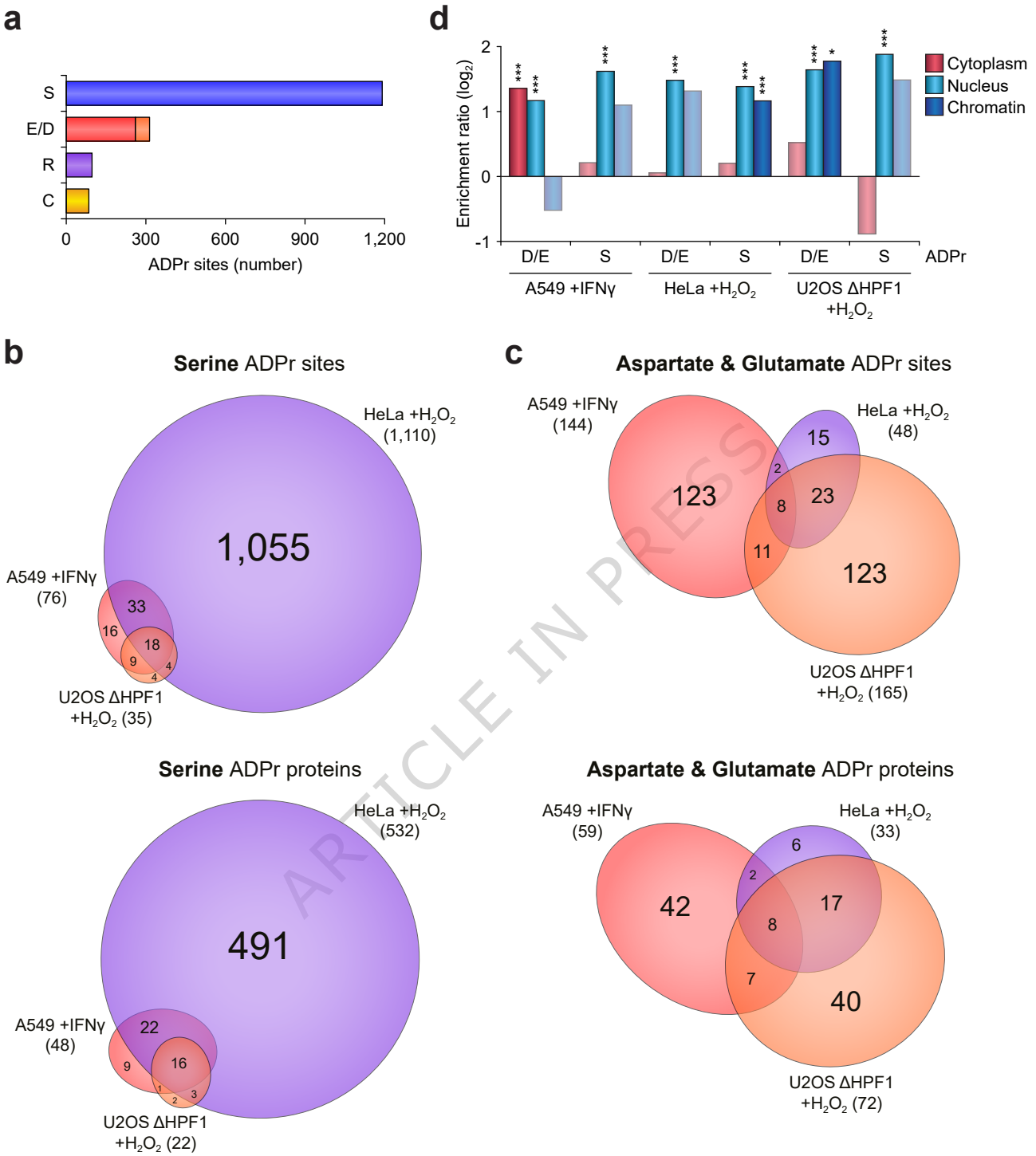

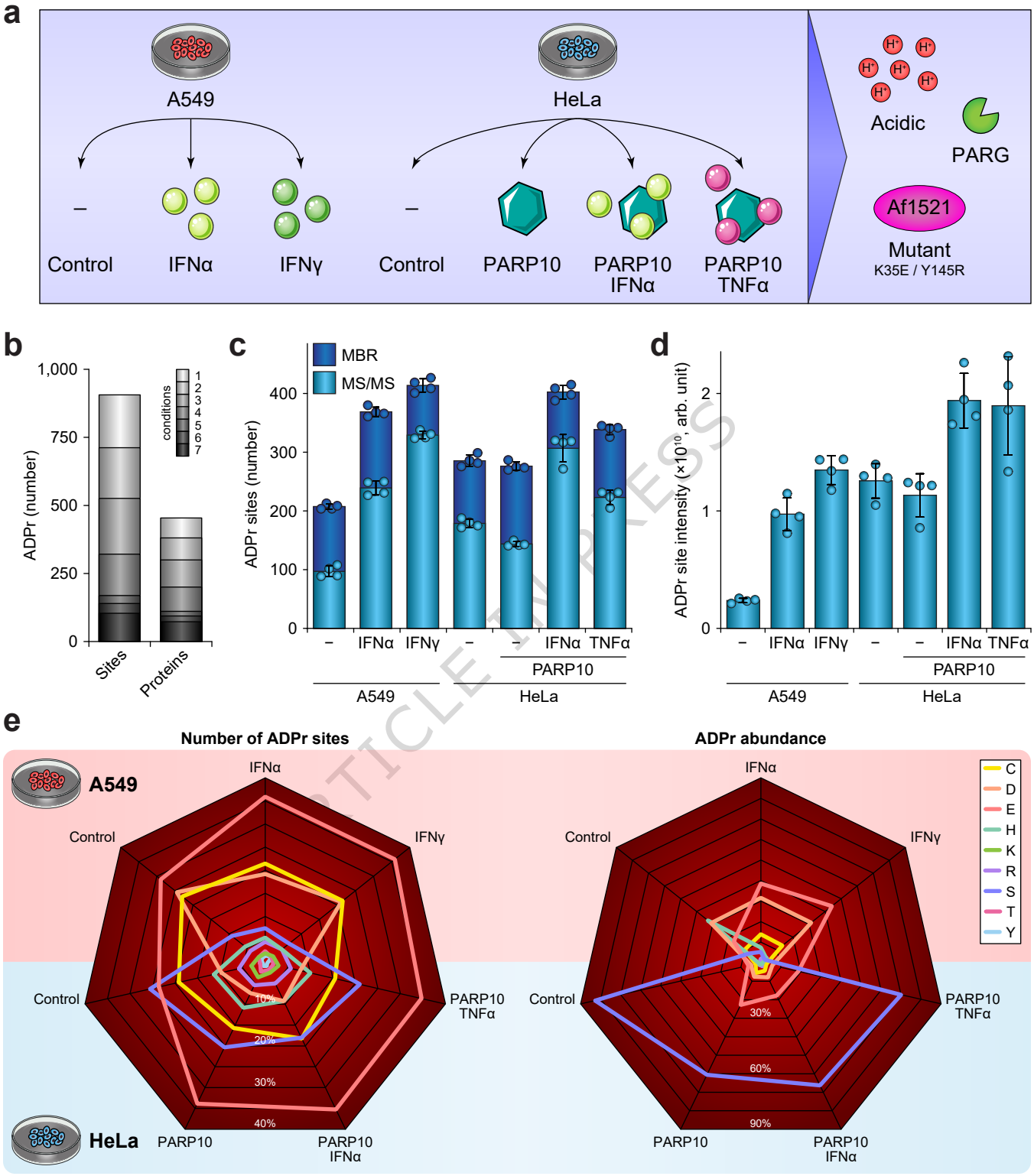
a
A549
HeLa
–
Control
IFNα
IFNγ
Control
PARP10
PARP10 IFNα
PARP10 TNFα
Acidic
PARG
Af1521
Mutant
K35E / Y145R
b
ADPr (number)
1,000
750
500
250
0
conditions
1
2
3
4
5
6
7
Sites
Proteins
c
MBR
MS/MS
ADPr sites (number)
400
300
200
100
0
– IFNα IFNγ – – IFNα TNFα
PARP10
A549
HeLa
d
ADPr site intensity (×10¹⁰, arb. unit)
2
1
0
– IFNα IFNγ – – IFNα TNFα
PARP10
A549
HeLa
e
Number of ADPr sites
ADPr abundance
A549
HeLa
IFNα
Control
IFNγ
PARP10
PARP10 TNFα
PARP10 IFNα
10%
20%
30%
40%
60%
90%
C
D
E
H
K
R
S
T
Y

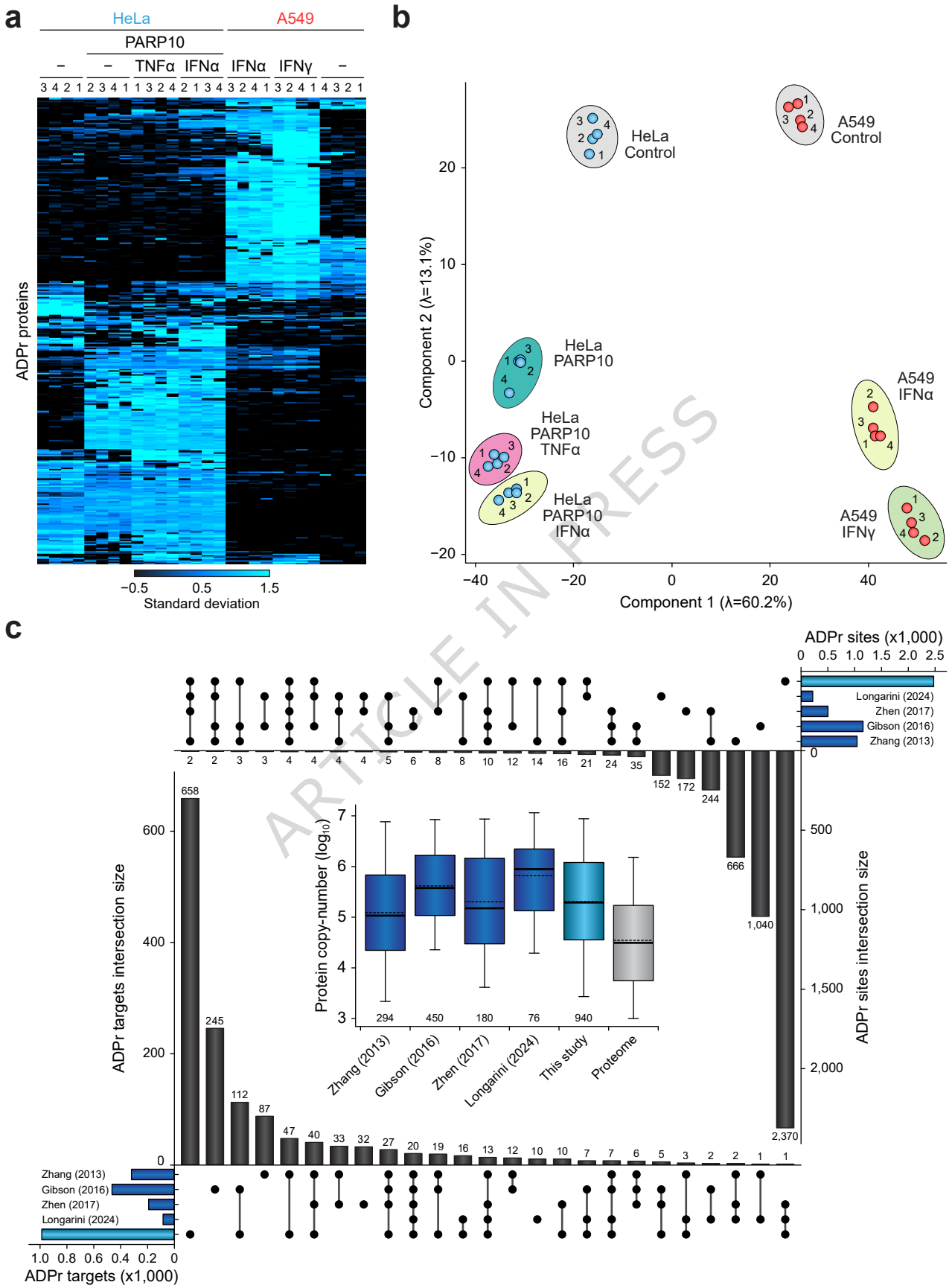

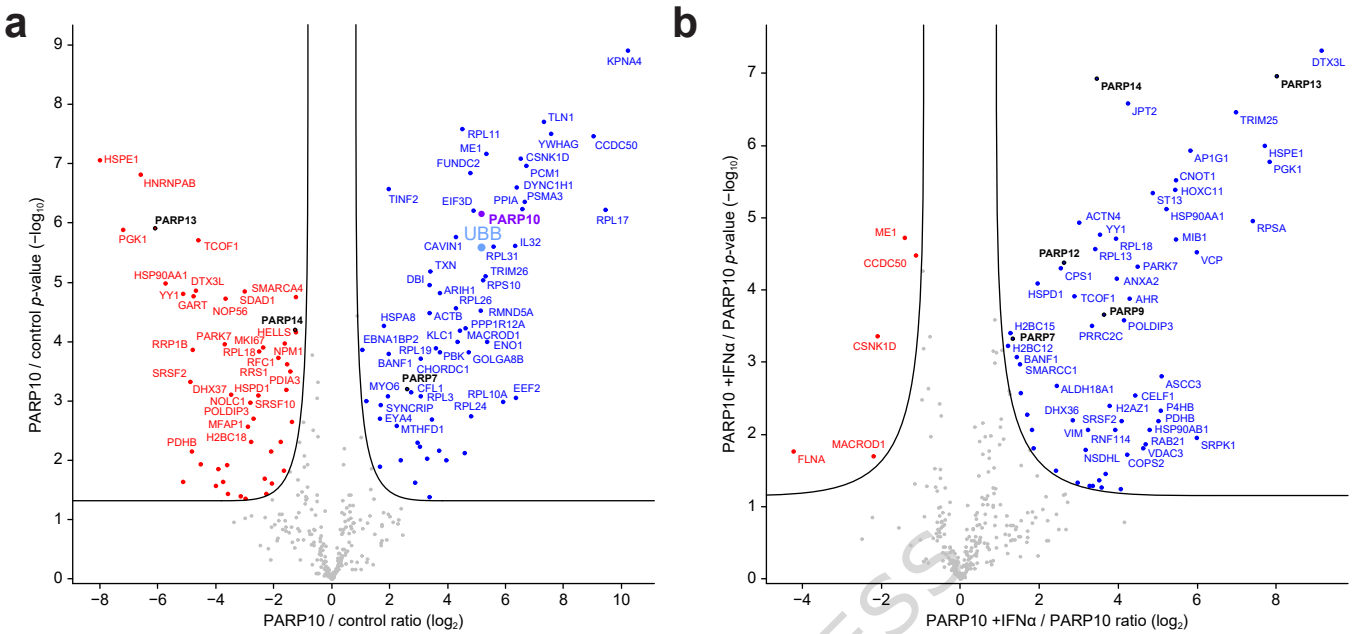

c

Protein	# sites DE	# sites S	Intensity %DE	Intensity %S	PARP10 / C ratio (log_2)
PARP1	17	11 4	220	1.5 99	−0.53
UBB	12	9 0	84	89 *n.d.*	**+5.17**
H4	10	4 2	57	32 63	−0.69
H2B	17	2 5	11	2.2 94	−0.50
H3.3	3	0 1	5.7	*n.d.* 97	−0.85

d

ADPr site	Control	PARP10
E-16	8.8	22
E-18	1.3	210
E-24	*n.d.*	810
D-32	7.7	1,600
K-33	2.6	560
E-34	8.0	63
E-51	130	4,800
R-54	3.0	11
D-58	53	*n.d.*
R-74/CT	720	320

f

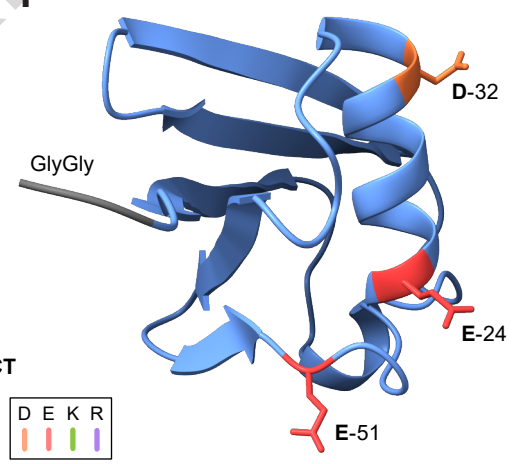

e

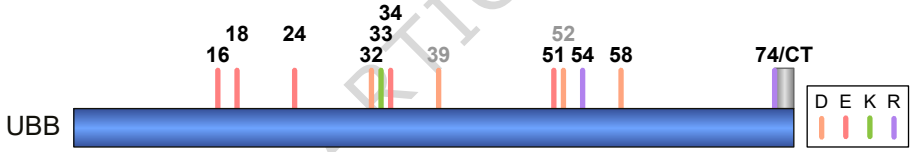

g